

Manufacturing of high-precision surface microstructures on stainless steel by ultrasonic impact peening

Xuesen Zhao

Harbin Institute of Technology

Dongxu Zhao

Harbin Institute of Technology

Wangjie Hu

Harbin Institute of Technology

Junjie Zhang (✉ zhjj505@gmail.com)

Harbin Institute of Technology <https://orcid.org/0000-0002-9636-5551>

Xiaohui Wang

University of Jinan

Jianguo Zhang

Huazhong University of Science and Technology

Tao Sun

Harbin Institute of Technology

Research Article

Keywords: Surface texturing, Stainless steel, Ultrasonic impact peening, Diamond cutting, Finite element simulation.

Posted Date: April 12th, 2021

DOI: <https://doi.org/10.21203/rs.3.rs-396707/v1>

License: © ⓘ This work is licensed under a Creative Commons Attribution 4.0 International License.

[Read Full License](#)

Manufacturing of high-precision surface micro-structures on stainless steel by ultrasonic impact peening

Xuesen Zhao¹, Dongxu Zhao¹, Wangjie Hu¹, Junjie Zhang^{1,*}, Xiaohui Wang^{2,*}, Jianguo Zhang^{3,*}, Tao Sun¹

¹Center for Precision Engineering, Harbin Institute of Technology, Harbin 150001, China

²School of Mechanical Engineering, University of Jinan, Jinan 250022, China

³State Key Laboratory of Digital Manufacturing Equipment and Technology, School of Mechanical Science and Engineering, Huazhong University of Science and Technology, Wuhan 430074, China

Corresponding author: Junjie Zhang (zhjj505@gmail.com); Xiaohui Wang (me_wangxh1@ujn.edu.cn);

Jianguo Zhang (zhangjg@hust.edu.cn).

Abstract: Ultrasonic impact peening (UIP) is not only a mature technique of surface treatment, but also a promising method of surface texturing for promoting performance and functionalities of components and devices. In the present work, we demonstrate the feasibility of applying UIP in the manufacturing of high precision surface micro-structures on 316L stainless steel using a YG6 cemented carbide tool. Specifically, analytical investigation of the material deformation map under UIP is carried out, which is validated by corresponding finite element simulations based on a combined nonlinear isotropic/kinematic hardening model, as well as experiments performed on home-made UIP apparatus. Finally, surface micro-structures of aligned grooves with a depth of 2 μm and a periodicity of 240 μm are fabricated by using UIP, and are subsequently subjected to linear reciprocating ball-disk sliding tests. Corresponding experimental results show that the micro-structures fabricated by UIP possess comparable accuracy of groove morphology and frictional properties with that fabricated by using ultrasonic elliptical vibration cutting using a single crystal diamond tool. The present work sheds lights on

the low-cost fabrication of high precision surface micro-structures on ferrous metals by mature UIP technique.

Keywords: Surface texturing; Stainless steel; Ultrasonic impact peening; Diamond cutting; Finite element simulation.

1 Introduction

Surface texturing is a promising technique for enhancing performance and functionality of components and devices by introducing micro/nano-scale surface structures. For instance, significant friction reduction between rubbing surfaces has been achieved by introducing micro-structures on stainless steel, which is a kind of widely used industrial engineering material for mechanical components [1-6]. Apart from the resultant enhanced tribological properties, how to effectively fabricate micro-structures with high accuracy on the ferrous metal of stainless steel is still intriguing.

The non-traditional laser surface texturing (LST) has been widely used to fabricate microstructures on stainless steel for its high efficiency, high homogeneity and low material-selectivity [7-11]. However, it is still challenging for LST to maintain high accuracy for fabricating microstructures with depths below a few microns, in particular for the low cost nanosecond pulsed laser micromachining due to pronounced heat-affected zone [12-13]. Recently, ultra-precision diamond cutting has been demonstrated as one feasible traditional mechanical machining technique for the fabrication of high precision micro-structures on stainless steel [15-16]. However, the machinability of stainless steel by diamond cutting is greatly limited by the severe tool wear of diamond tool due to strong diffusion between carbon and iron [17-19]. Although the method of ultrasonic elliptical vibration cutting (UEVC) can significantly promote the machinability of difficult-to-cut materials [20-24], it requires high precision and high cost machining apparatus, as well as high requirement on operating skills.

For instance, expensive components such as aerostatic bearing spindle and natural single crystal diamond are indispensable in UEVC. Therefore, a low cost technique for the fabrication of stainless steel micro-structures with uncompromised high accuracy is greatly needed.

Ultrasonic impact peening (UIP) is a widely used technique of cold surface treatment for increasing fatigue life and/or decreasing residual stress of welded metallic parts [25-28]. Based on the effect of high frequency oscillation impacts of treated part surface by high energetic needles, harmful tensile residual stresses in the top layer of treated surface are relieved. Consequently, the resultant compressive residual stress formation and metallographic structures refinement jointly lead to enhanced performance and mechanical properties of treated parts. Apart from the surface treatment purpose, UIP is also applied in the machining of metallic materials. For instance, a mirror surface of stainless steel with surface roughness of 0.1 μm can be directly achieved by using UIP [29-30]. However, the feasibility of low cost fabrication of stainless steel surface micro-structures by using UIP has not been explored. Although permanent plastic deformation-induced surface micro-structures fabrication by using UIP with increased oscillation amplitude could be expected, there are questions raised but not yet answered: Whether high precision surface micro-structures can be fabricated on stainless steel by controlling permanent plastic deformation behavior in UIP? If yes, what're the underlying formation mechanisms of as-fabricated structures?

Revealing involved mechanisms such as material deformation and correlated surface micro-structure formation is crucial to facilitate the feasibility of micro-structure fabrication by using UIP. In particular, the underlying deformation behavior of workpiece material in UIP and UEVC is significantly different from each other. Specifically, work hardening of workpiece material in UIP is more pronounced than that in UEVC due to the absence of material removal. Consequently, the configuration of finite element (FE) simulation, which serves as an important supplementary to experimental study, is of significant difference between UIP and UEVC. Specifically, the widely used Johnson-Cook constitutive law for FE simulations of metal cutting

[31-33] may be not proper to fully describe the work hardening behavior of materials under UIP, due to the overestimation of surface residual stress under cyclic loading conditions [34]. The combined isotropic-kinematic hardening model has been successfully applied to describe material behavior under cyclic loading conditions. Zheng et al. built a FE model based on the combined isotropic kinematic material plasticity model to investigate the effect of ultrasonic impact treatment on residual stress of 304L stainless steel weld joints, and found that the predicted distributions and magnitude of residual stress agree well with experimental results [35]. Liu et al. developed a FE model of ultrasonic surface rolling of 40Cr that implements the combined non-linear isotropic kinematic hardening model, which is capable of providing consistent predictions of surface layer nanocrystallization, residual stress and work hardening with experimental results [36]. However, the feasibility of applying the combined isotropic-kinematic hardening model in the surface micro-structures fabrication by using UIP has not yet been reported. Thus, developing an accurate FE model based on the combined isotropic-kinematic hardening model is essentially required for revealing underlying fundamental mechanisms involved in the UIP-based micro-structures fabrication.

Therefore, in the present work we investigate the feasibility of applying UIP in the surface micro-structures fabrication on 316L stainless steel. Specifically, the theoretical map of material deformation in UIP process is analytically investigated, and is validated by both FE simulations of UIP based on the combined isotropic/kinematic work hardening and experiments carried out on home-made UIP apparatus. Subsequently, fabrication of surface micro-structures composed of aligned grooves with a depth of 2 μm and a periodicity of 240 μm by using UIP is experimentally achieved. Furthermore, the formation accuracy and the tribological property of as-fabricated micro-structures by using UIP are compared with the same micro-structures fabricated by using UEVC.

2 Methodology

2.1 Experimental setup of UIP

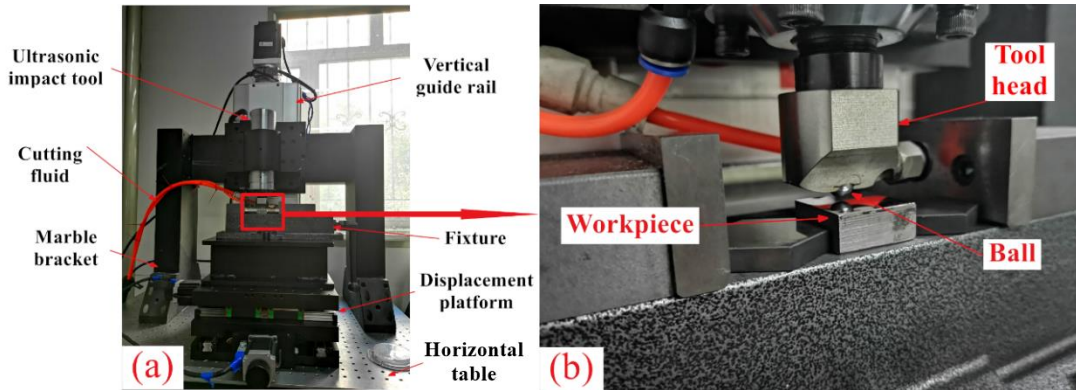


Fig. 1 Experimental setup of UIP apparatus. (a) Overall configuration; (b) enlarged view of tool-workpiece contact.

Fig. 1 shows the configuration of home-made apparatus of UIP, which mainly consists of two parts, as an ultrasonic impact tool and a three-dimensional motion stage, respectively. The ultrasonic impact tool contains an ultrasonic transducer and a YG6 cemented carbide ball with a diameter of 8 mm. The ultrasonic transducer converts input electrical energy into mechanical energy with ultrasonic waves, which result into the oscillations of the ball with a constant frequency of 27 KHz and an amplitude of 6 μm . The ultrasonic impact tool is fixed with the vertical linear guideway of the motion stage, while the specimen is statically fixed on the two-directional crossed horizontal guideways of the motion stage.

Fig. 2 illustrates the UIP-based microstructure fabrication process. Specifically, the specimen surface contacted with the ball moves precisely by the horizontal movements of two-directional crossed guideways according to pre-determined motion strategy, while keeping the vertical oscillation of the ball. Table. 1 lists the utilized machining parameters in UIP process, which are determined from the specifications of the home-made UIP apparatus. The specimen

material is a cold-rolled austenitic 316L stainless steel with an average grain size of 15 μm , which has a Young's modulus of 192 GPa and a yield strength of 300 MPa. We note that the initial states of the specimen, such as treatment methods and metallographic structures, would have a strong impact on the deformation-dominated UIP process. The specimen has a dimension of 20 mm in length, 20 mm in width and 10 mm in height. Prior to UIP, the stainless steel is grounded to a mirror surface with a surface roughness of 0.1 μm and a flatness of 1 μm . The morphology and surface profile of specimen is characterized by a Zeiss Merlin Compact scanning electron microscope (SEM) and a surface profilometer of Mitutoyo SurfTest SJ210, respectively. The profilometer has a tip radius of 5 μm and a tip angle of 90° with a measuring force of 4 mN, which resolves 2 nm vertically.

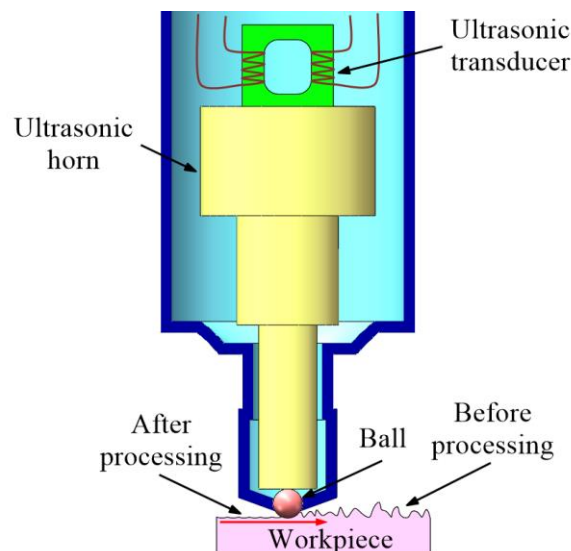


Fig. 2 Schematic diagram of surface micro-structures fabrication by using UIP.

Table. 1 Machining parameters used in UIP and UEVC

Parameters	UIP	UEVC
Frequency (kHz)	25	41.6
Amplitude (μm)	6	4

Feed (μm)	240	20
Velocity (m/min)	2	1
Cutting depth (μm)	6	6
Tool parameter	YG6 cemented carbide	Single crystalline diamond
	Diameter of 8 mm	Rake angle 0° , clearance angle 10° , nose radius 1 mm

2.2 FE modeling of UIP

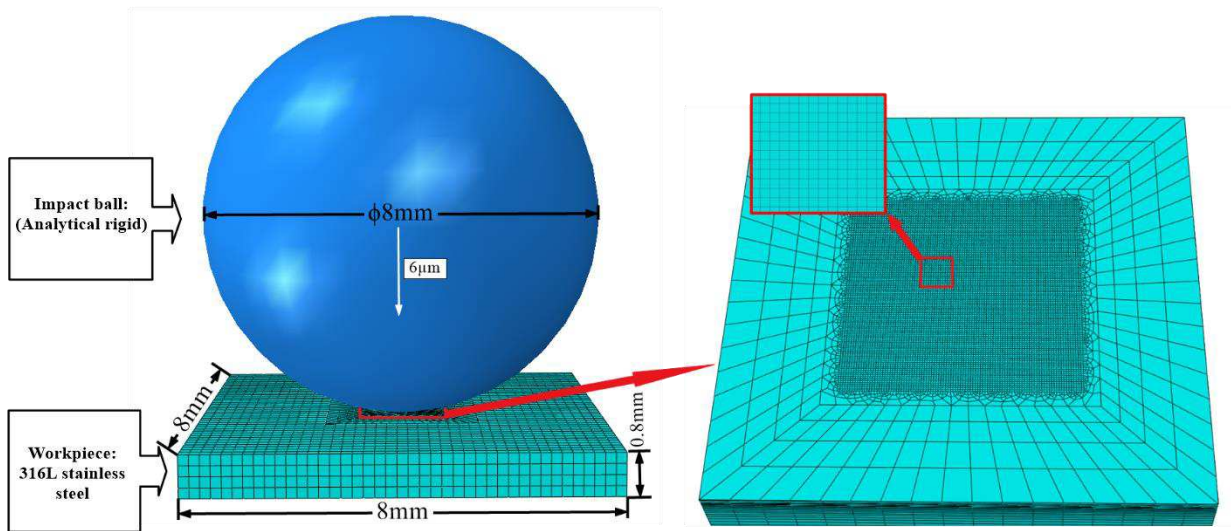


Fig. 3 3D FE model of UIP.

Fig. 3 shows the 3D FE model of UIP-based surface micro-structures fabrication, which contains a stainless steel specimen and a YG6 cemented carbide ball. The specimen has a dimension of 8 mm in length, 8 mm in width and 0.8 mm in height. And the target region subjected to UIP has a dimension of 1.48 mm in length, 1.48 mm in width and 0.8 mm in height. The target region is meshed by C3D8R elements. The minimum mesh size adopted in the FE model of UIP is closely related with the size of single impact indentation on specimen surface. Klemenz et al. demonstrated that the smallest element size should be one-tenth of the diameter of a single impact indentation, for ensuring the prediction accuracy of the FE simulation of high frequency impact indentation [37]. While the diameter of the impact ball is 8 mm and the

indentation depth is 6 μm , the theoretically calculated diameter of a single impact indentation is 438 μm . Therefore, the minimum mesh size is set to 15 $\mu\text{m} \times 15 \mu\text{m} \times 2 \mu\text{m}$, corresponding to 30 units in each impact indentation. Furthermore, a configuration of transition elements is applied in the rest of the specimen except for the target region. The impact ball is treated as an analytical rigid body for its higher hardness of 1424 HV than that of 156 HV for 316L stainless steel.

To be consistent with the UIP experiments, in the FE simulations of UIP the ball impacts the target surface with a frequency f of 25 KHz and an amplitude A of 6 μm . Since ultrasonic impact is generated by ultrasonic transducer converting electrical energy with sinusoidal form of alternating current into mechanical energy, in the FE simulations of UIP the mechanical vibration of the ball follows a form of harmonic vibration, which is expressed in Eq. (1):

$$Y = A\sin(\omega t - \varphi) \quad (1)$$

where Y is a vertical position, ω is vibration period and φ is shift angle that is zero in the current study. In the micro-structures fabrication process, the impact ball moves with a constant speed of 20 mm/s.

In the ultrasonic impact process, the specimen undergoes severe elastoplastic deformation under the cyclic impacting with ultrasonic frequency. In order to describe the significant work hardening of the material under UIP, a constitutive model considering combined nonlinear isotropic/kinematic hardening under cyclic loading is utilized. The isotropic hardening component σ^0 , which describes an equivalent force change that defines the size of yield surface, is expressed in Eq. (2):

$$\sigma^0 = \sigma|_0 + Q_\infty(1 - e^{-b\bar{\varepsilon}^{pl}}) \quad (2)$$

where $\sigma|_0$ is the initial stress at zero plastic strain, Q_∞ is the maximum change in the size of yield surface, $\bar{\varepsilon}^{pl}$ is a function of equivalent plastic strain, and b is the strain range at which the stress-strain curve is obtained. The non-linear kinematic hardening component describes the

backstress-induced translation of yield surface in stress space. The overall backstress α is composed of multiple backstress components α_k , which can be described in Eq. (3):

$$\alpha = \sum_{k=1}^N \alpha_k \quad (3)$$

where the evolution of backstress components $\dot{\alpha}_k$ is defined as Eq. (4):

$$\dot{\alpha}_k = C_k \dot{\bar{\epsilon}}^{pl} \frac{1}{\sigma^0} (\sigma - \alpha) - \gamma_k \alpha_k \dot{\bar{\epsilon}}^{pl} + \frac{1}{C_k} \alpha_k \dot{C}_k \quad (4)$$

where C_k is the initial kinematic hardening moduli, γ_k is related to the rate at which the kinematic hardening modulus decreases with the increase of plastic deformation, \dot{C}_k is the change rate of C_k with respect to temperature and field variables, and $\dot{\bar{\epsilon}}^{pl}$ is a function of equivalent plastic strain. Table. 2 lists utilized parameters of the non-linear isotropic/kinematic hardening model for 316L stainless steel, which are successfully utilized to describe ratchetting process of 316L stainless steel under tension-torsion loadings [38].

Table. 2 Parameters of non-linear isotropic/kinematic hardening model for 316L stainless steel.

N	σ^0 (MPa)	C_1 (MPa)	γ_1	C_2 (MPa)	γ_2	Q_∞ (MPa)	b
2	300	10125	1051	6546	81	120	13.2

2.3 Experimental setup of UEVC

In addition to UIP, surface micro-structures fabrication by using UEVC with a diamond tool is also conducted. By precisely controlling the motion of machine tool itself in the cutting depth direction, the envelope of cutting edge can be precisely transferred to machined surface, which leads to successfully fabrication of micro-/nano-structures. In the present work, the diamond tool elliptically vibrates with a vibration frequency of 41.6 kHz and an amplitude of 4 μm in both the cutting direction and the cutting depth direction. With the pick feed of 20 μm , each micro-nano structure is fabricated within 12 cutting cycles. Table. 1 also lists the utilized parameters for micro-structures fabrication by using UEVC. The detailed description can be

found elsewhere [22]. FE simulation of UEVC of 316L stainless steel is also performed. The basic configuration of the specimen is the same with that used in FE simulation of UIP. The specific details of FE modeling of UEVC can be referred to Ref. [39].

2.4 Experimental setup of friction test

The as-fabricated surface micro-structures on 316L stainless steel by using both UIP and UEVC are subjected to linear reciprocating ball-on-disk sliding tests on the Bruker CTER-UMT-3 tribometer. The counterbody is a GCr15 steel ball with a diameter of 4 mm. The specimen is completely immersed into a lubricant of non-additive poly-alpha-olefin oil (PAO 40) for 30 minutes to achieve full fluid film lubrication before each sliding test. The test direction is perpendicular to the groove direction. Real-time friction coefficient, defined as the ratio of friction force to normal load after the running-in period, is recorded. For each specimen, three repeated sliding tests with the same friction conditions are performed. The duration of each sliding test is 10 minutes, the stroke length is 10 mm, the normal load is 1.5 N and the sliding speed is 10 mm/s. The detailed description about the friction test can also be found elsewhere [10].

3 Results and discussion

3.1 Analytical investigation of UIP

The morphology and residual stress profile of groove microstructures fabricated by using UIP are analytical investigated. Fig. 4(a) presents the cross-sectional profile of as-fabricated grooves. Given the ultrashort duration of impact ball oscillations, the ball feed can be treated as sequential impact events. Specifically, the ball firstly impacts the specimen surface with specified frequency and amplitude in individual impact events, which lead to formation of dimple structures. And the height of previously formed dimple is lowered by the intersection of

adjacent dimple. Therefore, sequential impact events lead to the formation of a groove composed of dimples with reduced height.

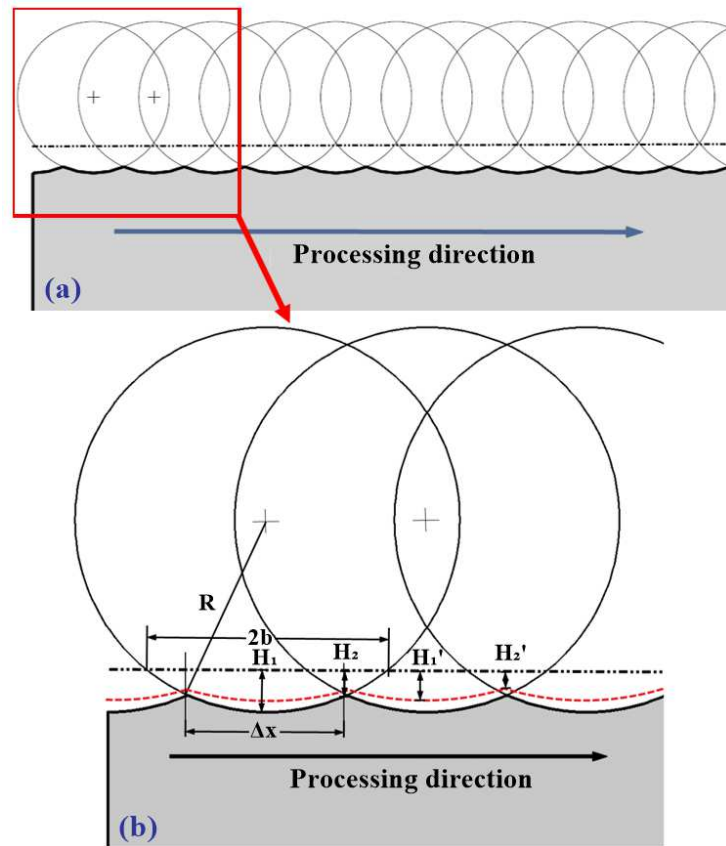


Fig. 4 Schematic diagram of UIP processing. (a) Holistic diagram of sequential impact events; (b) Enlarged view of sequential impact events.

Wang et al. demonstrated that high intensive dislocation slip is one dominant deformation mechanisms of 316L stainless steel under UIP, which leads to significant grain refinement [40]. XX et al. experimentally correlated the valleys formed by UIP with deformationability of treated materials [41]. Fig. 4(b) shows the enlarged view of three sequential impact events, in which black dash line refers to the original surface prior to UIP, black line indicates the specimen surface at the maximum deformation amount in the loading stage, and red dashed line is the specimen surface after unloading.

Due to the ultrashort duration of 0.04 ms for one loading cycle, the contact between ball and specimen surface can be treated as a continuous status. Therefore, the maximum deformation amount of the specimen H_1 is equal to the displacement of the ball A , i.e., $H_1 =$

A. In the case of without the consideration of plastic recovery, the distance of the local groove peak resulted by the intersection of two adjacent dimples to the original surface can be derived based on the geometrical relationship expressed in Eq. (5):

$$H_2 = H_1 - R + \sqrt{R^2 - \left(\frac{\Delta x}{2}\right)^2} \quad (5)$$

where R is the diameter of the ball, and $\Delta x = \frac{V_x}{f}$ is the distance between two peaks, in which V_x represents the transverse feed speed. The contact length $2b$ at the end of loading stage with the maximum deformation amount in one impacting event can be deduced by Eq. (6):

$$2b = 2\sqrt{R^2 - (R - H_1)^2} \quad (6)$$

However, plastic recovery plays an important role in UIP due to significant work hardening. Big-Alabo et al. theoretically investigated the material deformation in impact process and found that the amount of plastic recovery is $\left(\frac{3F_c}{4E^*R^2}\right)^{\frac{2}{3}}$, where F_c represents the contact force at the maximum deformation amount [42]. $E^* = \frac{E}{1-\nu^2}$ represents the effective elastic modulus for a rigid ball with an infinite large hardness, where E and ν represents the Young's modulus and the Poisson's ratio of the specimen material, respectively. Therefore, with the consideration of plastic recovery of the impacted surface, the maximum irreversible deformation amount H'_1 is expressed in Eq. (7):

$$H'_1 = H_1 - \left(\frac{3F_c}{4E^*R^2}\right)^{\frac{2}{3}} \quad (7)$$

And the distance of the peak resulted by two adjacent impacts to the original surface H'_2 can be derived from Eq. (8):

$$H'_2 = H_2 - \left(\frac{3F_c}{4E^*R^2}\right)^{\frac{2}{3}} \quad (8)$$

Therefore, the distance from peaks to groove bottom ΔH can be derived by Eq. (9):

$$\Delta H = H'_2 - H'_1 = \sqrt{R^2 - \left(\frac{V_x}{2f}\right)^2} - R \quad (9)$$

Regardless of material plastic flow and other factors, the surface roughness Ra of the groove bottom can be simplified as $Ra = \frac{\Delta H}{2}$, which has the magnitude of a few nanometer. Big-Alabo et al. reported that the material deformation in impact process can be simplified into three stages, as elastic deformation, (linear) elastoplastic deformation and complete plastic deformation, respectively [42]. Accordingly, the contact force F_c in the three stages can be deduced from Eq. (10):

$$F_c = \begin{cases} \frac{4}{3} E^* R^{\frac{1}{2}} H_1^{\frac{3}{2}} & H < H_y & \text{elastic deformation} \\ \frac{4}{3} E^* R^{1/2} [(H_1 - H_y)^{3/2} + H_y^{3/2}] & H_y < H < H_p & \text{elastoplastic deformation} \\ \pi R \sigma_y (4.6H_1 + H_p - 2.8H_y) & H > H_p & \text{complete plastic deformation} \end{cases} \quad (10)$$

where $H_y = \frac{0.681\pi^2 R \sigma_y^2}{E^2}$ represents the deformation amount at yielding point, σ_y is the yielding stress of the specimen material. $H_p = 7.84H_y$ represents the maximum amount of elastoplastic deformation [43]. The average contact stress σ_c can be expressed in Eq. (11):

$$\sigma_c = \frac{F_c}{\pi b^2} = \frac{F_c}{\pi H_1 (2R - H_1)} \quad (11)$$

According to Hertz contact theory, the contact-induced compressive stress distribution of a rotating body $\sigma(r)$ can be expressed in Eq. (12):

$$\sigma(r) = \sigma_m \left(1 - \frac{r^2}{b^2}\right)^{\frac{1}{2}} \quad (12)$$

Therefore, the contact force at the maximum deformation F_c can also be derived from Eq. (13):

$$F_c = \int_0^b \sigma(r) 2\pi r dr = \frac{2}{3} \sigma_m \pi H_1 (2R - H_1) \quad (13)$$

where r is the horizontal distance of contacting point to the ball center, and σ_m is the maximum contact force as $\sigma_m = \frac{3}{2} \sigma_c$. Therefore, the contact stress σ_1 at H_1 can be expressed in Eq.

(14):

$$\sigma_1 = \sigma_m = \frac{3}{2}\sigma_c \quad (14)$$

3.2 FE simulation validation of analytical model of UIP

To validate the analytical results of UIP summarized in Section 3.1, FE simulation of UIP that contains only single impact within one loading cycle is performed. Be consistent with the theoretical process of UIP, the FE simulation of single impact process includes two stages of loading and following unloading. In the loading stage, the ball penetrates into the specimen surface until a maximum displacement of 6 μm is reached within 0.02 ms. In the subsequent unloading stage, the impact ball is withdrawn from the specimen to its original position. The trajectory of the ball in the loading stage follows the Eq. (1). After the unloading stage, the ball continuously moves upwards for 10 μm to allow for stress relaxation.

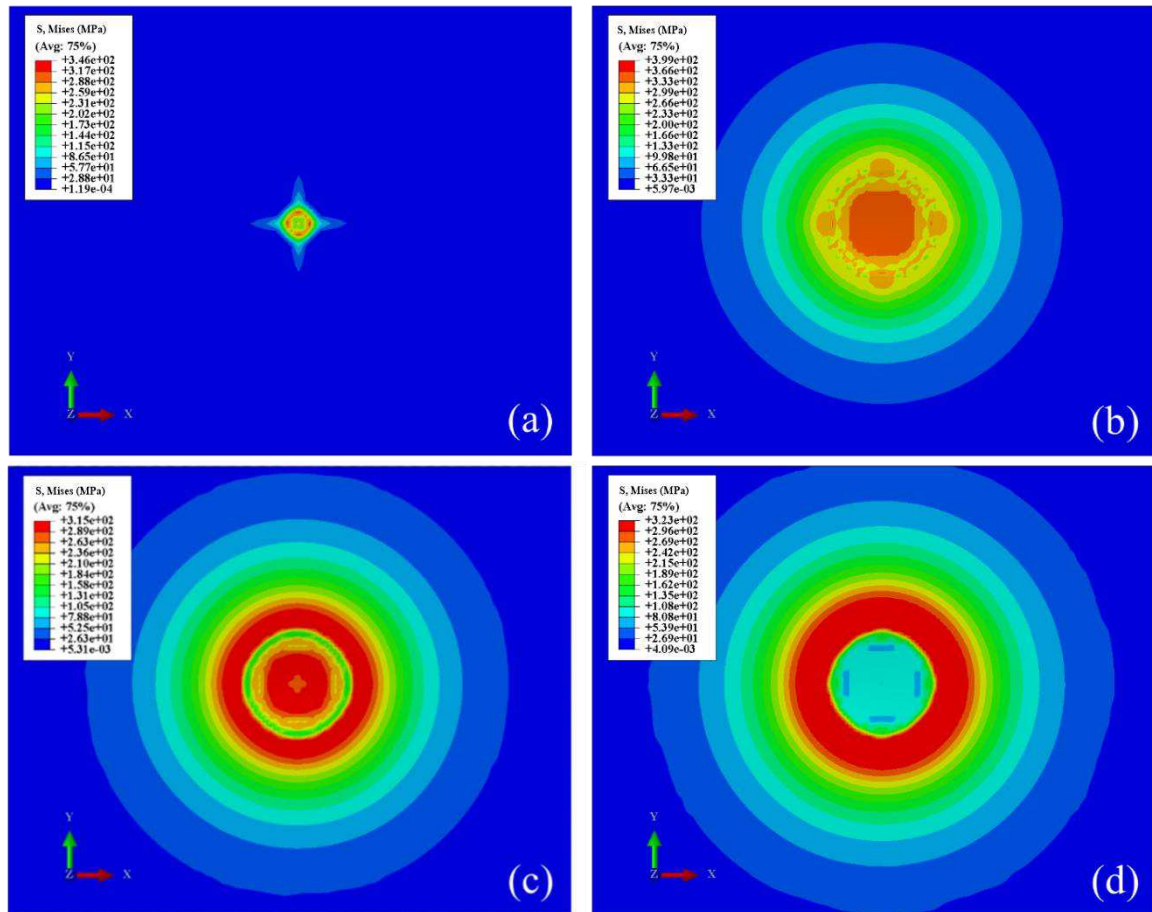


Fig. 5 FE simulation results of surface evolution in single impact process. a) Start of loading stage; b) End of loading stage; c) Initial period of unloading stage; d) End of unloading stage.

Fig. 5 presents the contours of Mises stress distribution on the treated specimen surface by the FE simulation. In the loading stage, Fig. 5(b) shows that the contact stress distribution is centered around the contact center with circular symmetry, and expands with increased contact area accompanied with the increase of penetration depth. Fig. 5(c) shows that significant stress relaxation is occurred in the unloading stage. After the complete separation of the ball from specimen surface, there is residual stress within the top layer observed, as shown in Fig. 5(d).

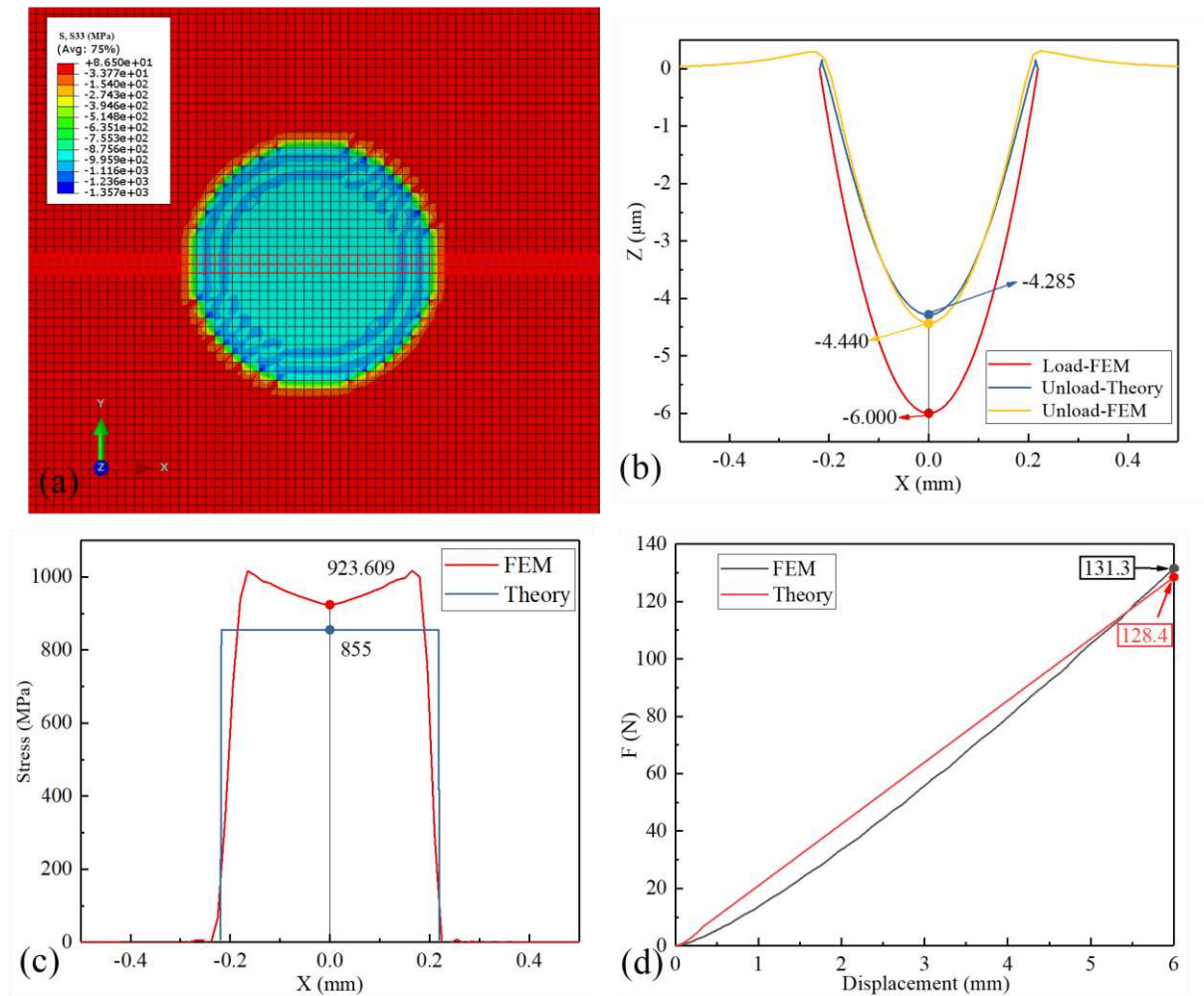


Fig. 6 Analytical investigation and FE simulation of single impact process. (a) distribution of vertical stress; (b) Comparison of groove profile; (c) Cross-sectional stress profile of contacted surface; (d) Contact force.

Fig. 6(a) shows the vertical stress distribution on the workpiece surface at the end of loading stage by the FE simulation. And Fig. 6(b) shows groove profiles, in which red and yellow line represents the profile at the end of loading stage and unloading stage, respectively.

Fig. 6(b) demonstrates a significant plastic recovery of approximate 2 μm of treated surface after fully unloading. The profile of the groove after unloading derived from analytical analysis is also presented by the blue line in Fig. (b). It is seen from Fig. 6(b) that the maximum irreversible deformation amount of the contact area by FE simulation is 4.44 μm , which has an error of 3.64% to the theoretical value of 4.285 μm derived from Equ. (7). Fig. 6(c) shows the contact stress contour of the specimen-ball contact interface at the end of loading stage, demonstrating the consistence between FE simulation (red curve) and analytical investigation (blue curve). Specifically, FE simulation shows that the maximum contact stress occurred at the groove bottom is 923.6 MPa, which has a deviation of 8% from the theoretical value of 855 MPa.

Fig. 6(d) shows the variation of contact force with tool displacement during the single impact process, in which the red and black line corresponds to analytical investigation and FE simulation, respectively. Fig. 6(d) indicates that the contact forces predicted by analytical investigation and FE simulation are in good agreement with each other. Specifically, the maximum contact force after loading is 128.4 N for analytical investigation, which has an deviation of 2.3% from 131.3 N for FE simulation. Therefore, FE simulation results are in good agreement with theoretical results, in terms of the maximum unrecoverable deformation amount and contact stress distribution.

In addition to single impact process, FE simulations of groove formation by continuous impact process are also carried out. The feed speed of the impact ball is 20 mm/s, the amplitude is 6 μm , the vibration frequency is 25 kHz, and the distance between neighboring grooves is 300 μm . Fig. 7 presents sequential evolution of treated surface morphology. It can be seen from Fig. 7(b) that the initial period of the first groove processing is accompanied with material accumulation occurred in the feed direction, which becomes more pronounced with the feed of the ball. It can be seen from Fig. 7(b) that the material deformation is caused by the combined action of the vertical impact and the horizontal rolling of the ball. Material accumulation is an important factor that affects the accuracy of micro-structure topography. In addition, it can be

seen from Fig. 7(c) that the processing of the second groove interferes with the shape of the previous one, leading to the reduction of the width of the first groove. However, Figs. 7(c) and (d) show that both the topographies of the second and third grooves are not uniform, which is caused by the influence of accumulation of displaced materials.

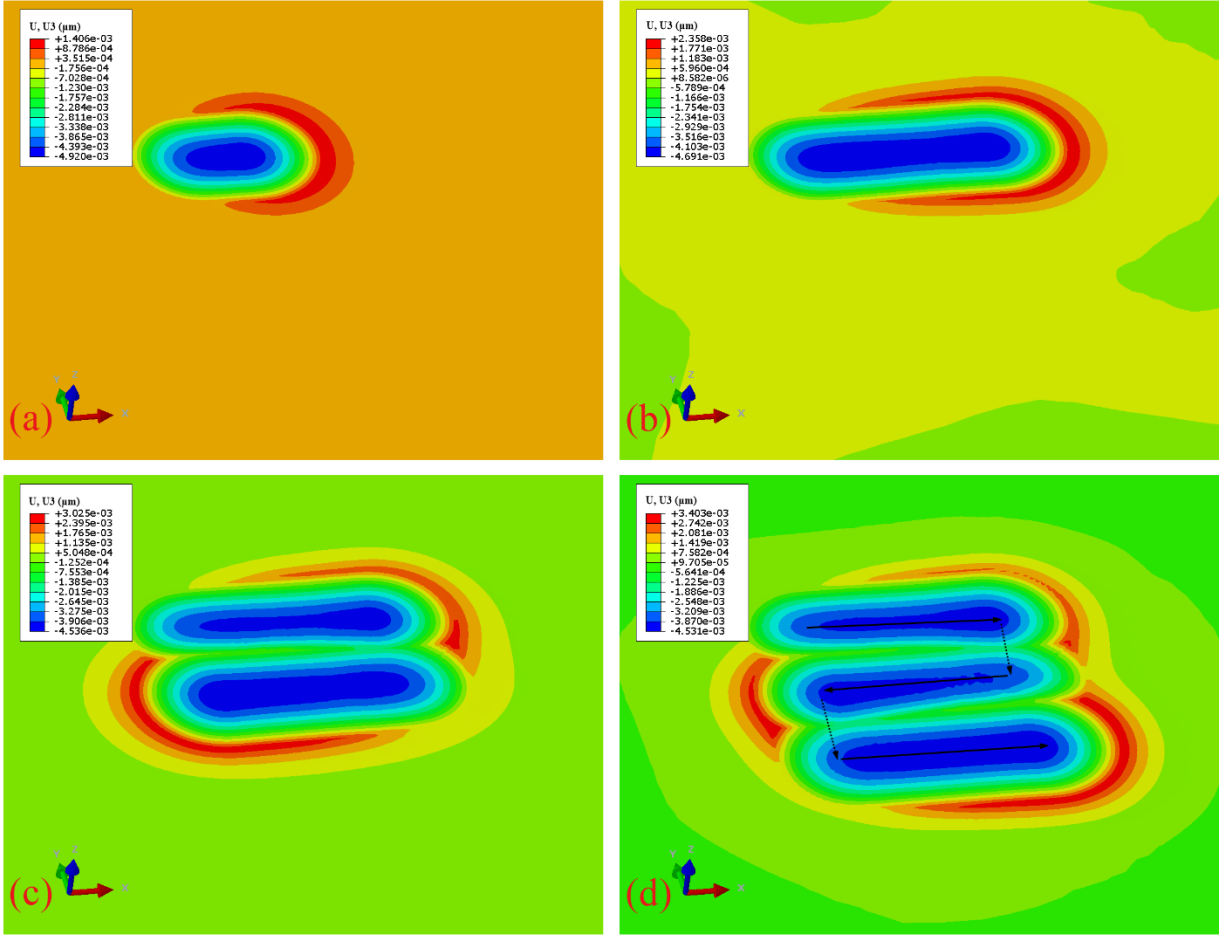


Fig. 7 FE simulation of surface morphology evolution in continuous impact process. (a) Start processing, (b) one groove, (c) two grooves, (d) three grooves.

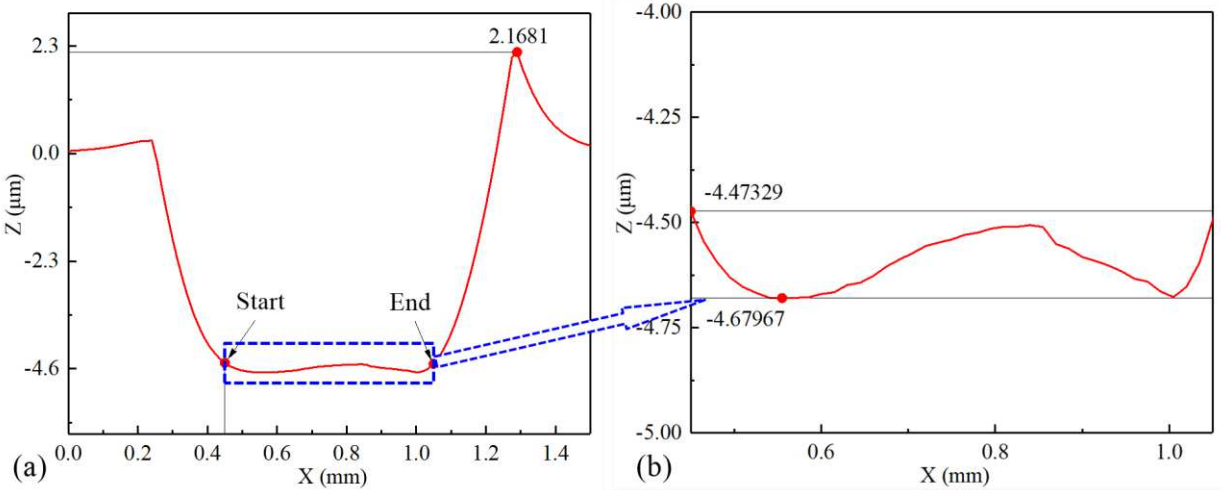


Fig. 8 Morphology of groove bottom surface by using UIP. (a) Groove profile along groove direction; (b) Enlarged view of groove bottom.

Fig. 8 plots the profile of the first groove bottom surface along groove direction obtained in the FE simulation. It is seen from Fig. 8(a) that the surface pile-up on the front side of the groove is more pronounced than that on the back side, which can be attributed to significant material accumulation in front of the ball and plastic recovery behind the ball. The maximum height of surface pile-up on the front side is 2.17 μm . In addition, it is seen from Fig. 8(b) that the deviation of groove bottom height is less than 0.2 μm , indicating a smooth morphology of groove bottom.

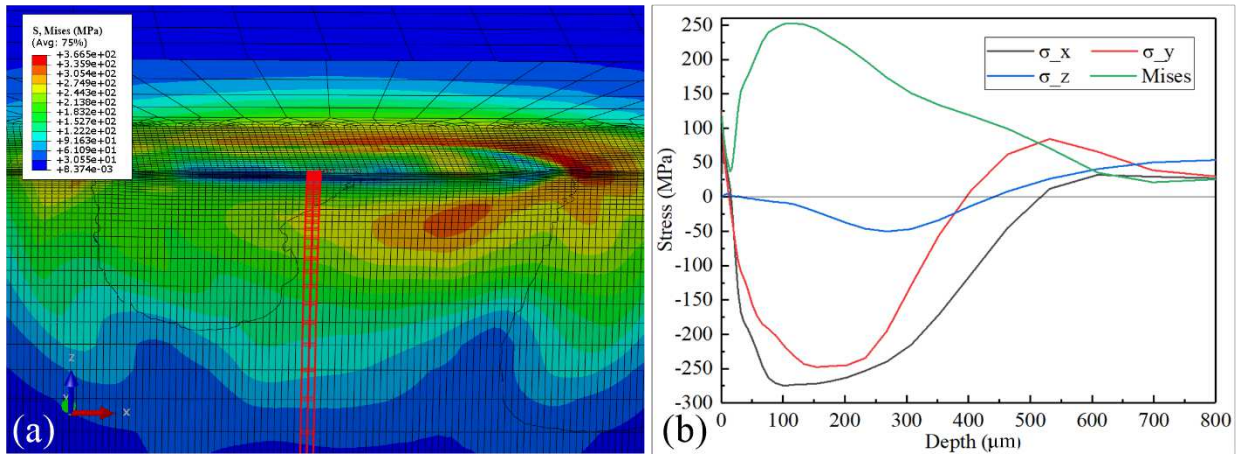


Fig. 9 Stress distribution at different depths at the groove bottom. (a) Mises stress distribution; (b) Variations of residual stress with depth.

Fig. 9 presents variations of residual stress components at the groove bottom along different directions with depth. It is seen from Fig. 9(b) that the residual stress in the X direction firstly decreases with increasing depth, and reaches a minimum value of -275 MPa at a depth of 100 μm , after which gradually increases with increasing depth. Furthermore, the residual stresses in the Y and Z directions have similar trends of variations with that in the Z direction. The residual stress in the Y and Z direction has a minimum value of -254 MPa at a depth of 150 μm and a minimum value of -50 MPa at a depth of 268 μm , respectively. Thus, Fig. 9 indicates that there are compressive residual stresses existed in the X, Y and Z directions of groove bottom when depth is not higher than 400 μm . Wang et al. also experimentally observed

considerable compressive residual stresses at the surface of 316L stainless steel treated by UIP [40].

3.3 Experiment validation of analytical model of UIP

To further validate the theoretical analysis and FE simulation results, single groove is experimentally fabricated on 316L stainless steel in the home-made UIP apparatus. The experimental machining parameters are the same with that used in the analytical investigation and FE simulation. Fig. 10(a) shows SEM image of as-fabricated single groove, indicating a smooth groove bottom surface with high surface integrity. The measured surface roughness of groove bottom is 5 nm. The width of as-fabricated groove is 477 μm , which has a deviation of 8.9% from the theoretical value of 438 μm . Fig. 10(b) shows the topography of the cross section of the groove. The depth of as-fabricated groove is 4.2837 μm , which has a deviation of less than 1% from the theoretical value of 4.285 μm , as well as a deviation of 3.52% from the value of 4.440 μm by FE simulation. And Fig. 10(b) also shows that the surface pile-up on the two side of the groove is not symmetrical. Specifically, the maximum height of surface pile-up on the right side of the groove is 2 μm , which has a deviation of 8.5% from the value of 2.17 μm by FE simulation.

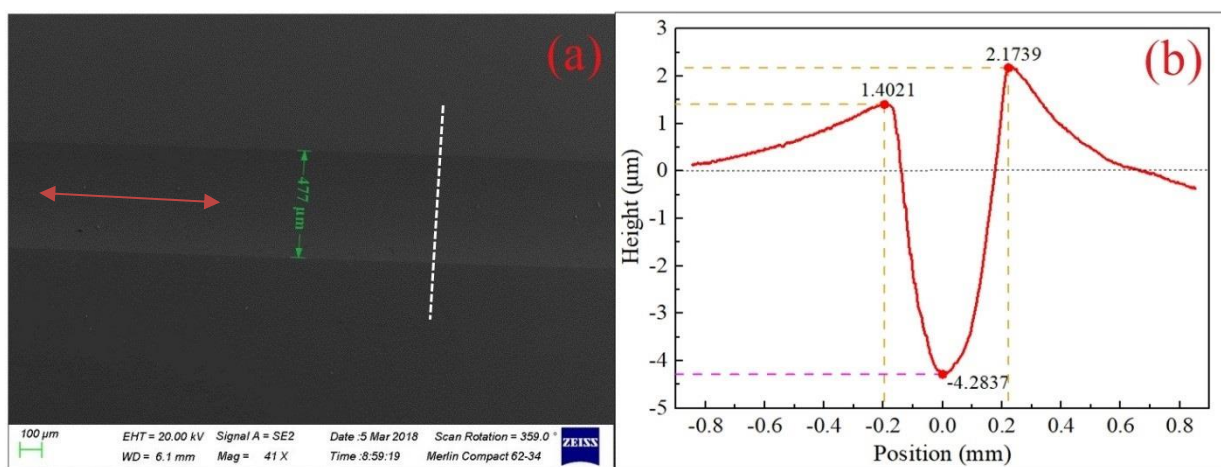


Fig. 10 Morphology of single groove by using UIP. (a) SEM image of groove morphology; (b) Groove profile.

3.4 Micro-structures fabrication by UIP

Above theoretical analysis, FE simulation and experimental work jointly demonstrate the feasibility of fabrication of high precision single groove micro-structure on 316L stainless steel by using UIP. Therefore, surface micro-structures composed of aligned grooves with a depth of 2 μm and a periodicity of 240 μm are fabricated on 316L stainless steel by using UIP with a YG6 cemented carbide tool. In addition, the same micro-structures are also fabricated by using UEVC with a single crystal diamond tool.

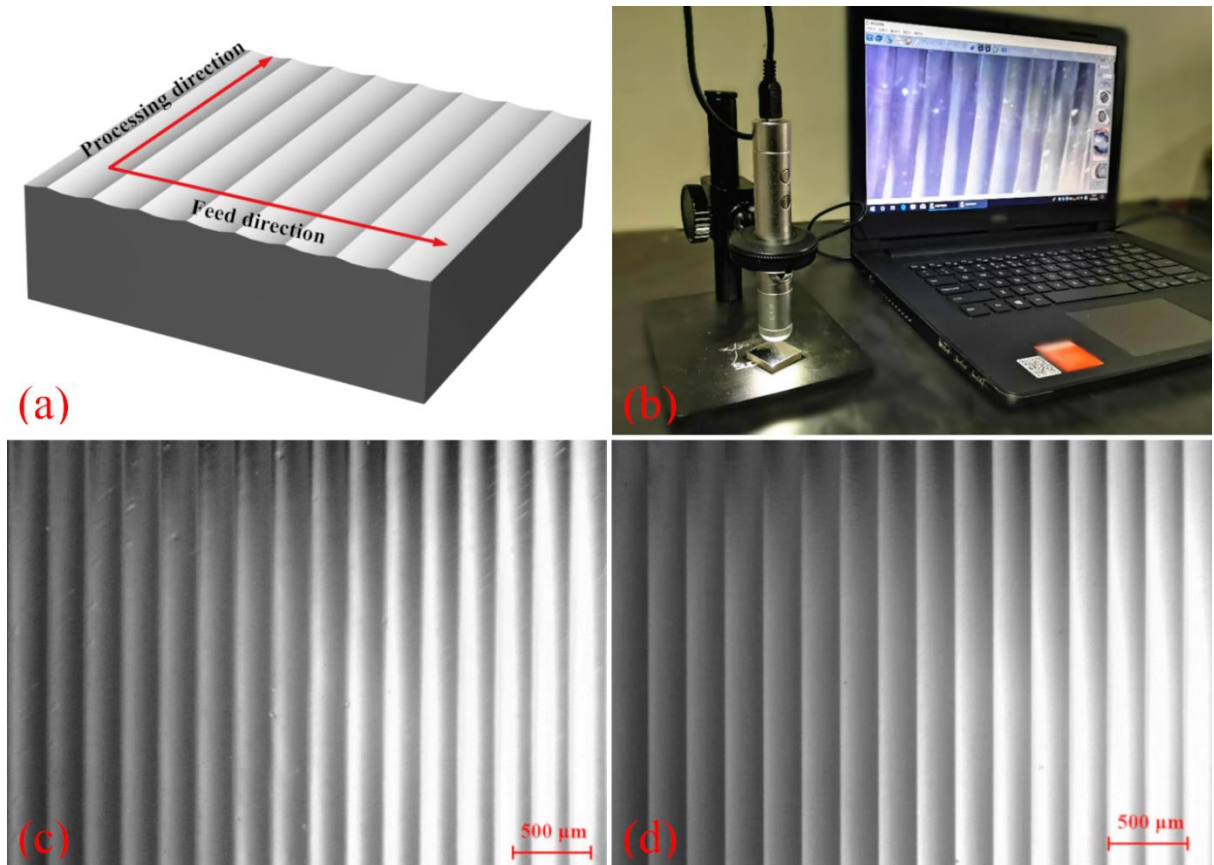


Fig. 11 Micro-structures composed of aligned grooves fabricated on 316L stainless steel. (a) Schematic illustration of micro-structures fabrication strategy; (b) Characterization of micro-structures by an optical microscopy; Fabricated micro-structures by using (c) UIP and (d) UEVC.

Fig. 11(a) illustrates the tool motion strategy employed in the micro-structures fabrication, which is the same for both UIP and UEVC. Specifically, the tool firstly moves in the processing direction to achieve the fabrication of the first groove, and then moves in the feed direction to

fabricate the neighboring second groove. By precisely controlling the feed of the tool, groove micro-structures with a depth of 2 μm can be fabricated by the intersection of adjacent grooves. A SuperEyes B011 optical microscope is utilized to characterize the surface image of the microstructures, as shown in Fig. 11(b). Accordingly, Fig. 11(c) and (d) shows the optical image of as-fabricated micro-structures by using UIP and UEVC, respectively, which both show well-aligned uniform grooves fabricated on stainless steel. Since a blunt spherical cutting edge is used in UIP, the resulting form accuracy of as-fabricated grooves by using UIP is lower than that by using UEVC with an ultra-sharp cutting edge. And there are also minor flaws observed on the micro-structures by using UIP.

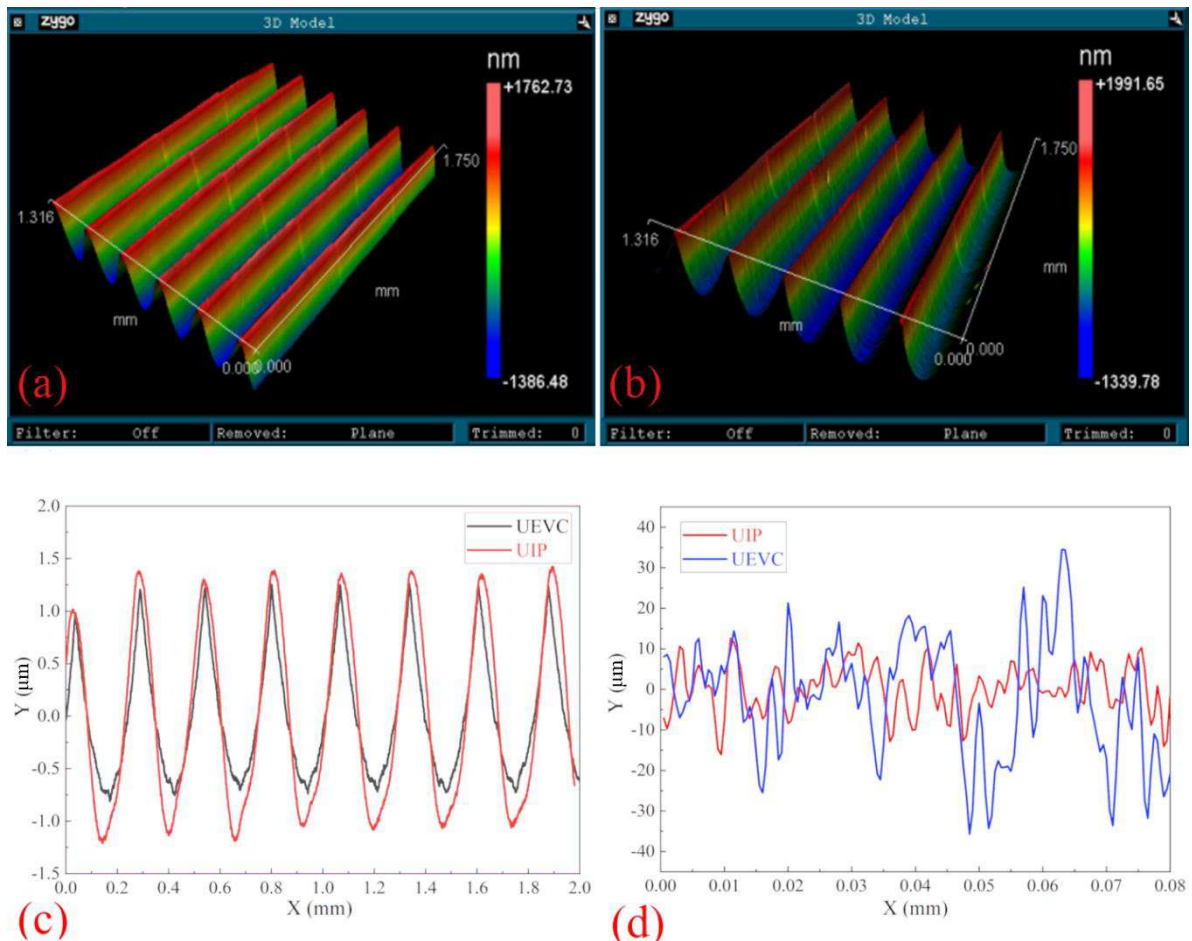


Fig. 12 Geometrical features of as-fabricated micro-structures on stainless steel. Morphology of groove by using (a) UIP and (b) UEVC; (c) Surface profile of grooves; (d) Variations of groove bottom surface height.

The geometrical features of as-fabricated micro-structures are further characterized by a Zygo white light interferometer. Fig. 12(a) and (b) presents morphology of as-fabricated

micro-structures by using UIP and UEVC, respectively, which shows long range uniformity of micro-structures for each method. Fig. 12(c) further plots surface profiles of micro-structures, which show a highly agreement in groove width for the two machining methods. However, the groove depth by using UIP is 2.14 μm , which is slightly higher than that of 1.92 μm by using UEVC. Furthermore, the groove uniformity by using UIP is better than that by using UEVC. Fig. 12(c) also demonstrates a sharper groove peak by UEVC than that by UIP, which is also attributed to different tool geometries used. Fig. 12(d) further plots variations of groove bottom surface height with groove length, which indicate less pronounced fluctuations by using UIP than that by using UEVC, thus suggesting a smoother groove bottom can be achieved by using UIP. Although above results indicate that high precision surface micro-structures can be successfully fabricated on 316L stainless steel by using UIP with the machining strategy shown in Fig. 11(a), the ratio of width to depth for the as-fabricated micro-structures is greatly limited, due to the small vertical vibration amplitude and the blunt spherical cutting edge.

3.5 Frictional properties of as-fabricated micro-structures

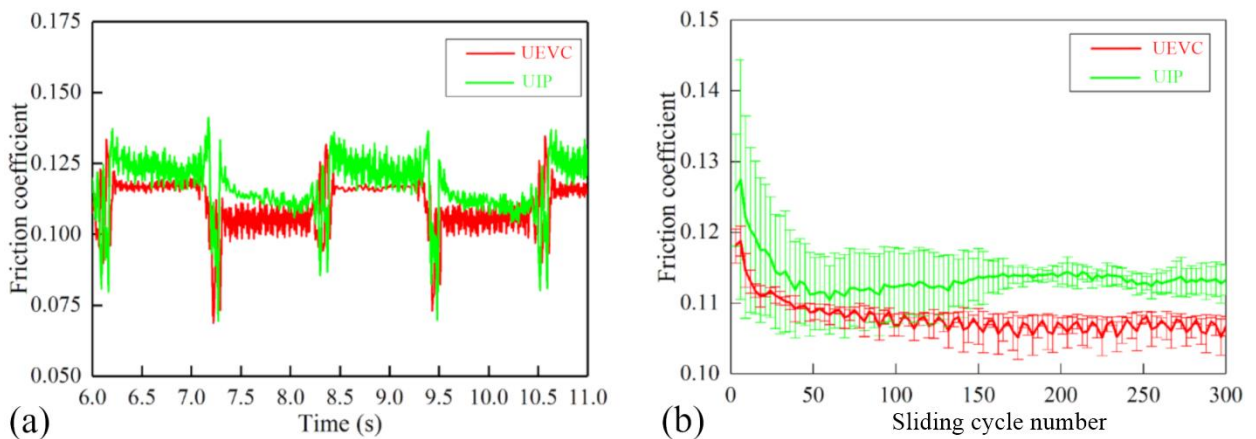


Fig. 13 Frictional properties of as-fabricated microstructures. (a) Variations of friction coefficient within 2 sliding cycles; (b) Variations of average friction coefficient within entire friction test of 300 sliding cycles.

The as-fabricated micro-structures by using both UIP and UEVC are subjected to linear reciprocating ball-disk sliding tests. Fig. 13(a) depicts the friction coefficient of as-fabricated

micro-structures in the first two sliding cycles after the running-in period. It is seen from Fig. 13(a) that the variation of friction coefficient for each method has similar characteristics. Specifically, friction coefficient fluctuates around constant values in both forward and backward sliding processes. Furthermore, the constant value in forwarding sliding process is larger than that in backward sliding process. However, the friction coefficient of the micro-structures by using UIP is slightly higher than that by using UEVC.

Fig. 13(b) further depicts variations of average friction coefficient with sliding cycle number in the entire sliding tests of the two micro-structures. The average friction coefficient is derived by averaging the friction coefficient in three repeated sliding tests, and corresponding error bars are also presented. It is seen from Fig. 13(b) that the variation of average friction coefficient for each machining method has similar features, as descending in the running-in period and then fluctuating around a constant value in the following stable sliding stage. However, the duration of running-in period is shorter for the micro-structures fabricated by using UEVC than that by using UIP. Furthermore, the constant friction coefficient for the micro-structures fabricated by using UEVC is 0.106, which is smaller than that of 0.113 by using UIP. The higher friction coefficient for the micro-structures fabricated by using UIP than that by using UEVC can be attributed to more serious work hardening occurred within treated material without material removal.

Fig. 14 presents FE simulation results of residual stress distributions within treated specimen surface after processing by using UIP and UEVC. It is seen from Figs. 14(a) and (b) that there are mainly residual compressive stresses existed on the specimen surface for the two machining methods. However, there are also considerable residual tensile stress existed on the surface for UIP, as demonstrated in Fig. 14(a). For UEVC, the residual tensile stress is mainly confined within the formed chip. Fig. 14(c) and (d) further quantitatively plots the variations of horizontal residual stress and vertical residual stress with machining length, respectively. Fig. 14(c) shows that the horizontal compressive residual stress for UIP ranges from 50 MPa to

150MPa. Hu et al. measured the residual stress of UIP-treated 316L welded butt-joint through blind-holes method, and found that the horizontal compressive residual stress is 95 MPa, which agrees well with the predicted values shown in Fig. 14 [44].

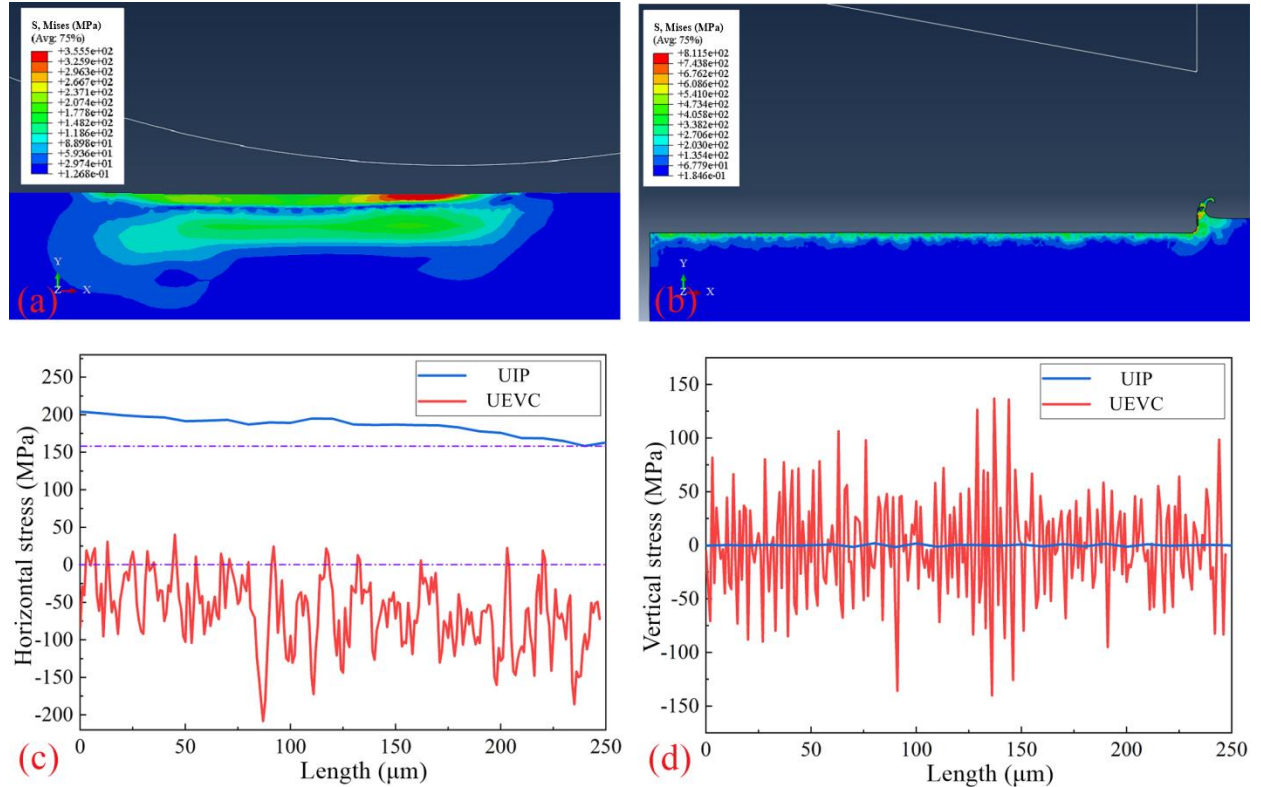


Fig. 14 Cross-sectional residual stress contour of specimen treated by using (a) UIP and (b) UEVC; Variation of residual stress in (c) horizontal stress and (d) vertical stress.

It is seen from Figs. 14(c) and (d) that there are small horizontal residual stress and large vertical stress generated on the surface for UEVC, as compared to that for UIP. In particular, the vertical stress for UIP is significantly reduced compared to that for UEVC, indicating a stable state of material deformation. Furthermore, the residual stresses in both horizontal and vertical directions for UIP have significantly less pronounced fluctuations than that for UEVC. The homogeneous distribution of residual stress for UIP can be mainly attributed to refinement of surface grains [45-46]. Rai et al. reported that the applying of UIP leads to grain refinement up to nano scale in surface region of 316L stainless steel, accompanied with enhanced mechanical properties such as microhardness, yield strength, tensile strength [45]. The existence of residual stress is closely related with mechanical properties of machined surface. Gale et al. showed that

the yield stress of DMLS 316L stainless steel treated by UIP is 37% higher than untreated one [47]. Therefore, the friction coefficient for UIP is larger than that for UEVC, due to more pronounced residual stress formed.

4 Summary

In summary, we demonstrate the feasibility of applying UIP in the fabrication of high precise surface micro-structure on 316L stainless steel using a YG6 cemented carbide tool. Specifically, the deformation map of the material in cyclic loading is analytical investigated, and the analyzed groove geometry and contact stress are validated by FE simulation of UIP based on a combined non-linear isotropic/kinematic hardening model. Meanwhile, single groove microstructure is fabricated on home-made UIP apparatus to further validate the theoretical and FE simulation results. Subsequently, surface micro-structures composed of aligned grooves with a depth of 2 μm and a periodicity of 240 μm are successfully fabricated on 316L stainless steel by using UIP, which are then subjected to linear reciprocating ball-disk sliding tests. The as-fabricated micro-structures by using UIP possess fairly comparable geometrical accuracy and frictional properties with the same micro-structures fabricated by using UEVC with a diamond tool.

Ethical Approval

Not applicable.

Consent to Participate

Not applicable.

Consent to Publish

Not applicable.

Authors contributions

Xuesen Zhao, Junjie Zhang and Jianguo Zhang conceived the project. Xuesen Zhao, Dongxu Zhao, Wangjie Hu and Tao Sun established the device; Dongxu Zhao and Xiaohui Wang performed the theoretical simulation. Dongxu Zhao, Junjie Zhang and Xiaohui Wang wrote the paper. All authors read and approved the final manuscript for the submission.

Acknowledgements

The authors greatly acknowledge the Open Research Foundation of State Key Laboratory of Digital Manufacturing Equipment and Technology in Huazhong University of Science and Technology, China (DMETKF2019016), National Natural Science Foundation of China (No. 51905194), the Science Challenge Project (No. TZ2018006-0201-02) and the Fundamental Research Funds for the Central Universities.

Competing Interests

The authors declare that they have no competing interests.

Data availability

The raw/processed data required to reproduce these findings cannot be shared at this time as the data also forms part of an ongoing study.

Reference

- [1] A. Ronen, I. Etsion, Y. Kligerman. Friction-reducing surface-texturing in reciprocating automotive components. *Tribology Transactions* 44 (2001) 359-366.
- [2] M. Wakuda, Y. Yamauchi. S. Kanzaki. Y. Yasuda. Effect of surface texturing on friction reduction between ceramic and steel materials under lubricated sliding contact. *Wear* 254 (2003) 356-363.
- [3] S. M. Hsu, Y. Jing, D. Hua, H. Zhang. Friction reduction using discrete surface textures: Principle and design. *Journal of Physics D-Applied Physics* 47(2014) 335307
- [4] J. Schneider, V. Djamiykov, C. Greiner. Friction reduction through biologically inspired scale-like laser surface textures. *Beilstein J. Nanotechnol.* 9 (2018) 2561-2572.
- [5] J. J. Zhang, J. G. Zhang, A. Rosenkranz, X. L. Zhao, Y. L. Song. Surface textures fabricated by laser surface texturing and diamond cutting - Influence of texture depth on friction and wear. *Advanced Engineering Materials* 20 (2018) 1700995
- [6] H. Kasem, O. Stav, P. Grützmacher, C. Gachot. Effect of low depth surface texturing on friction reduction in lubricated sliding contact. *Lubricants* 6 (2018) 62
- [7] X. L. Wang, K. Adachi, K. Otsuka, K. Kato. Optimization of the surface texture for silicon carbide sliding in water. *Applied Surface Science* 253 (2006) 1282-1286
- [8] I. Etsion, E. Sher. Improving fuel efficiency with laser surface textured piston rings. *Tribology International* 42 (2009) 542-547
- [9] D. Braun, C. Greiner, J. Schneider, P. Gumbsch. Efficiency of laser surface texturing in the reduction of friction under mixed lubrication. *Tribology International* 77 (2014) 142-147

- [10] J. J. Zhang, D. H. Yang, A. Rosenkranz, J. G. Zhang, L. Zhao, C. W. Song, Y. D. Yan, T. Sun. Laser surface texturing of stainless steel – effect of pulse duration on texture's morphology and frictional response. *Advanced Engineering Materials* 21 (2019) 1801016
- [11] A. Rosenkranz, H. L. Costa, F. Profito, C. Gachot, S. Medina, D. Dini. Influence of surface texturing on hydrodynamic friction in plane converging bearings - An experimental and numerical approach. *Tribology International* 134 (2019) 190-204
- [12] R. L. Harzic, N. Huot, E. Audouard, C. Jonin, P. Laporte, S. Valette, A. Fraczkiewicz, R. Fortunier. Comparison of heat-affected zones due to nanosecond and femtosecond laser pulses using transmission electronic microscopy. *Applied Physics Letters* 80 (2002) 3886
- [13] K. Sugioka, Y. Cheng. Ultrafast lasers—reliable tools for advanced materials processing. *Light: Science & Applications* 3 (2014) e149
- [14] E. Brinksmeier, R. Gläbe, J. Osmer. Ultra-precision diamond cutting of steel molds. *CIRP Annals* 55 (2006) 551-554.
- [15] H. Ni, Y. Wang, H. Gong, L. Pan, Z. J. Li, D. F. Wang. A novel free-form transducer for the ultra-precision diamond cutting of die steel. *The International Journal of Advanced Manufacturing Technology* 95 (2018) 2185-2192
- [16] Z. J. Li, F. Z. Fang, H. Gong, X. D. Zhang. Review of diamond-cutting ferrous metals. *The International Journal of Advanced Manufacturing Technology* 68 (2013) 1717-1731
- [17] B. M. Lane, T. A. Dow, R. Scattergood. Thermo-chemical wear model and worn tool shapes for single-crystal diamond tools cutting steel. *Wear* 300 (2013) 1-2
- [18] B. Chu, Y. F Shi, J. Samuel. Mitigation of chemical wear by graphene platelets during diamond cutting of steel. *Carbon* 108 (2016) 61-71

- [19] N. Furushiro, T. Yamaguchi, D. Hirooka, M. Shirakawa, S. Matsuda, Y. Iwasa, S. Terauchi. Effect of microstructure on mitigating tool wear in diamond turning of nitrided steels. *Precision Engineering* 54 (2018) 388-395
- [20] S. A. Sajjady, H. Nouri Hossein Abadi, S. Amini, R. Nosouhi. Analytical and experimental study of topography of surface texture in ultrasonic vibration assisted turning. *Materials & Design* 93 (2016) 311-323
- [21] X. Q. Zhang, K. Liu, A. S. Kumar, M. Rahman. A study of the diamond tool wear suppression mechanism in vibration-assisted machining of steel. *Journal of Materials Processing Technology* 214 (2014) 496-506
- [22] J. G. Zhang, N. Suzuki, Y. L. Wang, E. Shamoto. Ultra-precision nano-structure fabrication by amplitude control sculpturing method in elliptical vibration cutting. *Precision Engineering* 39 (2015) 86-99
- [23] L. Zou, Y. Huang, M. Zhou, L. Duan. Investigation on diamond tool wear in ultrasonic vibration-assisted turning die steels. *Materials and Manufacturing Processes* 32 (2017) 1505-1511
- [24] J. G. Zhang, J. J. Zhang. Frictional properties of surface textures fabricated on hardened steel by elliptical vibration diamond cutting. *Precision Engineering* 2019 In Press.
- [25] B. N. Mordyuk, G. I. Prokopenko. Ultrasonic impact peening for the surface properties' management. *Journal of Sound and Vibration* 308 (2007) 855-866
- [26] M. Malaki, H. Ding. A review of ultrasonic peening treatment. *Materials & Design* 87 (2015) 1072-1086
- [27] Y. Fan, X. Zhao, Y. Liu. Research on fatigue behavior of the flash welded joint enhanced by

ultrasonic peening treatment *Materials & Design* 94 (2016) 515-522

[28] J. Hu, T. Shimizu, T. Yoshino, T. Shiratori, M. Yang. Ultrasonic dynamic impact effect on deformation of aluminum during micro-compression tests. *Journal of Materials Processing Technology* 258 (2018) 144-154

[29] J. Marteau, M. Bigerelle, P. E. Mazeran. Relation between roughness and processing conditions of AISI 316L stainless steel treated by ultrasonic shot peening. *Tribology International* 82 (2015) 319-329

[30] M. Malaki, H. T. Ding. A review of ultrasonic peening treatment. *Materials & Design* 87 (2015) 1072-1086

[31] Y. C Zhang, J. C. Outeiro, T. Mabrouki. On the Selection of Johnson-cook Constitutive Model Parameters for Ti-6Al-4 V Using Three Types of Numerical Models of Orthogonal Cutting. *Procedia CIRP* 31 (2015) 112-117

[32] M. Daoud, J. F. Chatelain, A. Bouzid. Effect of rake angle on Johnson-Cook material constants and their impact on cutting process parameters of Al2024-T3 alloy machining simulation. *The International Journal of Advanced Manufacturing Technology* 81 (2015) 1987-1997

[33] F. Ducobu, E. R. Lorphèvre, E. Filippi. On the importance of the choice of the parameters of the Johnson-Cook constitutive model and their influence on the results of a Ti6Al4V orthogonal cutting model. *International Journal of Mechanical Sciences* 122 (2017) 143-155

[34] S. Bagherifard, R. Ghelichi, M. Guagliano. A numerical model of severe shot peening (SSP) to predict the generation of a nanostructured surface layer of material. *Surface and Coatings Technology* 204 (2010) 4081-4090

- [35] J. Zheng, A. Ince, L. Q Tang. Modeling and simulation of weld residual stresses and ultrasonic impact treatment of welded joints. *Procedia Engineering* 213 (2018) 36-47
- [36] Y. Liu, L. J. Wang, D. P. Wang. Finite element modeling of ultrasonic surface rolling process. *Journal of Materials Processing Technology* 211 (2011) 2106-2113
- [37] M. Klemenč, V. Schulze, I. Rohr, et al. Application of the FEM for the prediction of the surface layer characteristics after shot peening. *Journal of Materials Processing Technology* 209 (2009) 4093-4102
- [38] L. Portier, S. Calloch, D. Marquis, et al. Ratchetting under tension-torsion loadings: experiments and modelling. *International Journal of Plasticity* 16 (2000) 303-335
- [39] J. J. Zhang, L. Han, J. G. Zhang, et al. Brittle-to-ductile transition in elliptical vibration-assisted diamond cutting of reaction-bonded silicon carbide. *Journal of Manufacturing Processes* 45 (2019) 670-681
- [40] Z. D. Wang, G. F. Sun, Y. Lu, M. Z. Chen, K. D. Bi, Z. H. Ni. Microstructural characterization and mechanical behavior of ultrasonic impact peened and laser shock peened AISI 316L stainless steel. *Surface & Coatings Technology* 385 (2020) 125403.
- [41] J. Marteau, M. Bigerelle, P. –E. Mazeran, S. Bouvier. Relation between roughness and processing conditions of AISI316L stainless steel treated by ultrasonic shot peening. *Tribology International* 82 (2020) 319-329.
- [42] A. Big-Alabo, P. Harrison, M. P. Cartmell. Contact model for elastoplastic analysis of half-space indentation by a spherical impactor. *Computers and Structures* 151 (2015) 20-29
- [43] M. R. Brake. An analytical elastic-perfectly plastic contact model[J]. *International Journal of Solids and Structures* 49 (2012) 3129-3141

- [44] X. D. Hu, C. B. Ma, Y. C. Yang, Q. L. Zeng. Study on residual stress releasing of 316L stainless steel welded joints by ultrasonic impact treatment. *International Journal of Steel Structures* 20 (2020) 1014–1025.
- [45] P. K. Rai, V. Pandey, K. Chattopadhyay, L. K. Singhal, V. Singh. Effect of ultrasonic shot peening on microstructure and mechanical properties of high-nitrogen austenitic stainless steel. *Journal of Materials Engineering & Performance* 23 (2014) 4055–4064.
- [46] E. S. Statnikov, V. O. Muktepavel, A. Blomqvist. Comparison of ultrasonic impact treatment (UIT) and other fatigue life improvement methods. *Welding in the World* 46 (2013) 20–32.
- [47] J. Gale, A. Achuhan. Application of Ultrasonic Peening during DMLS production of 316L stainless steel and its effect on material behavior. *Rapid Prototyping Journal* 23 (2017) 1185-1194.

Figures

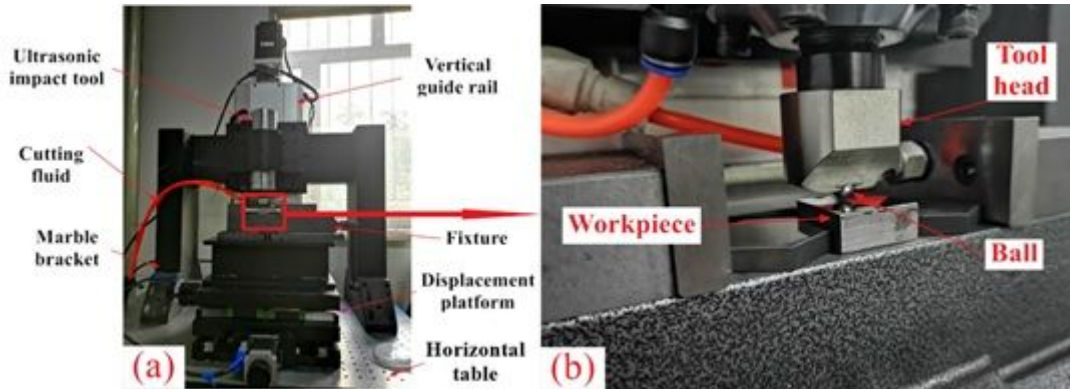


Figure 1

Experimental setup of UIP apparatus. (a) Overall configuration; (b) enlarged view of tool-workpiece contact.

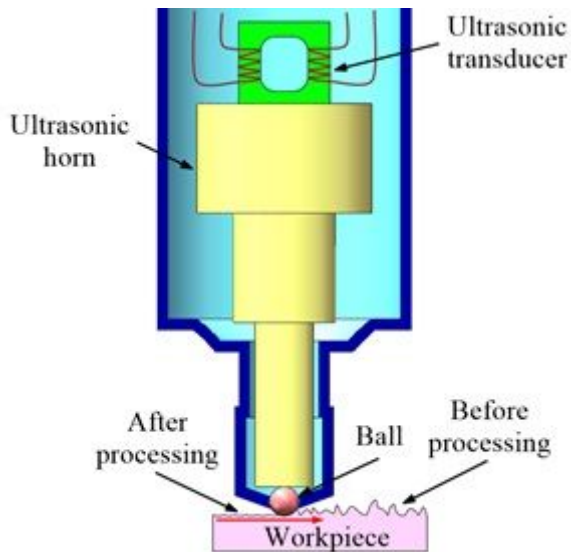


Figure 2

Schematic diagram of surface micro-structures fabrication by using UIP.

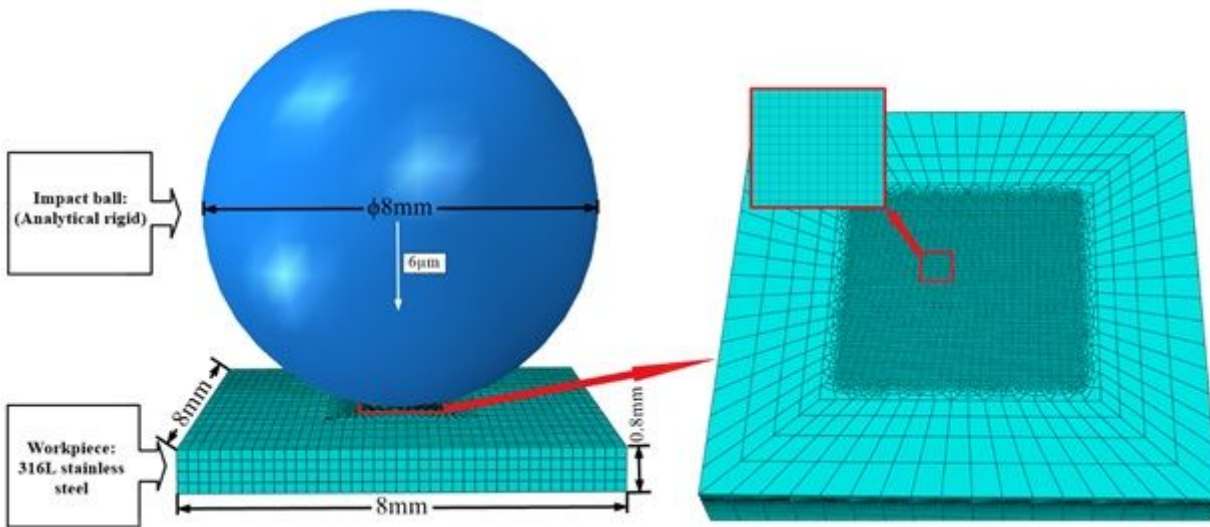


Figure 3

3D FE model of UIP.

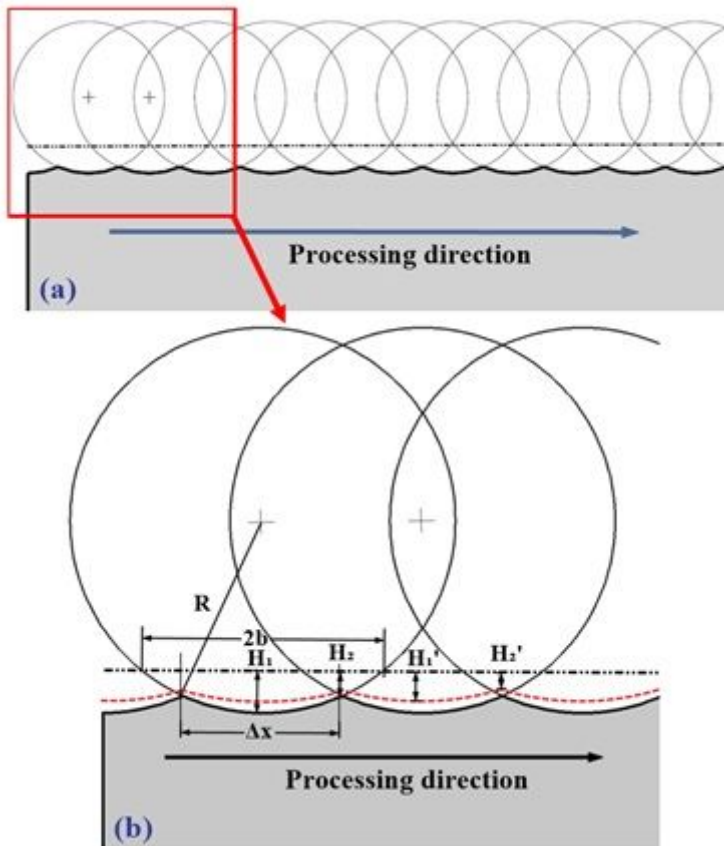


Figure 4

Schematic diagram of UIP processing. (a) Holistic diagram of sequential impact events; (b) Enlarged view of sequential impact events.

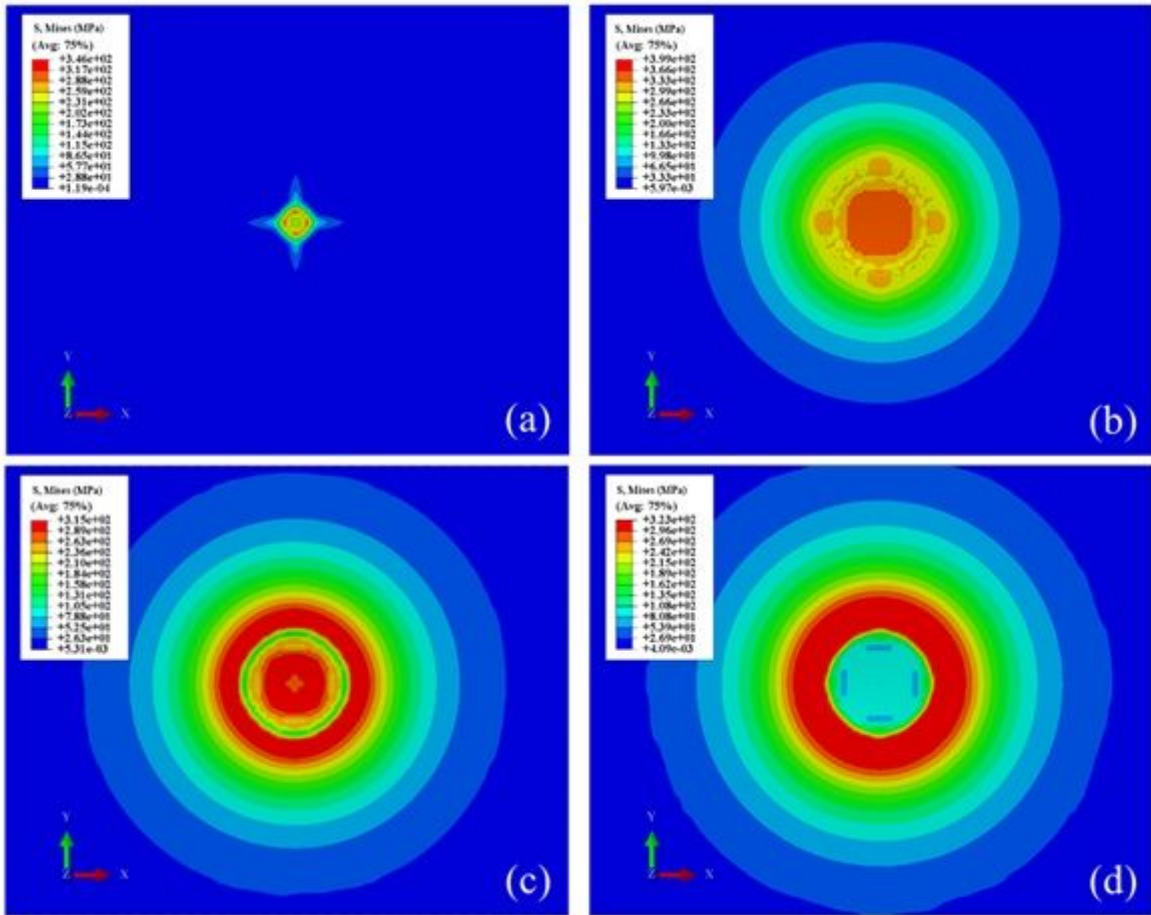


Figure 5

FE simulation results of surface evolution in single impact process. a) Start of loading stage; b) End of loading stage; c) Initial period of unloading stage; d) End of unloading stage.

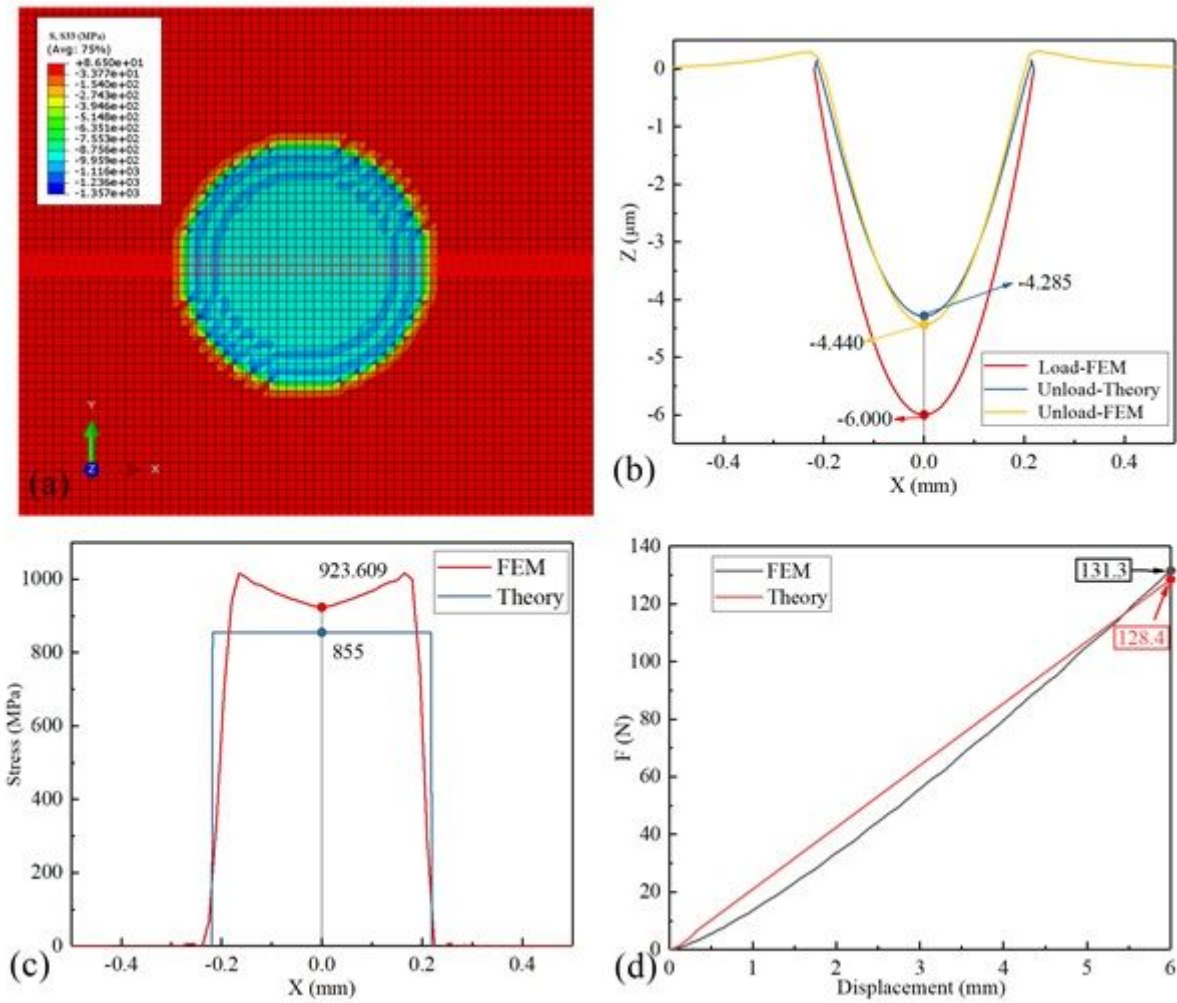


Figure 6

Analytical investigation and FE simulation of single impact process. (a) distribution of vertical stress; (b) Comparison of groove profile; (c) Cross-sectional stress profile of contacted surface; (d) Contact force.

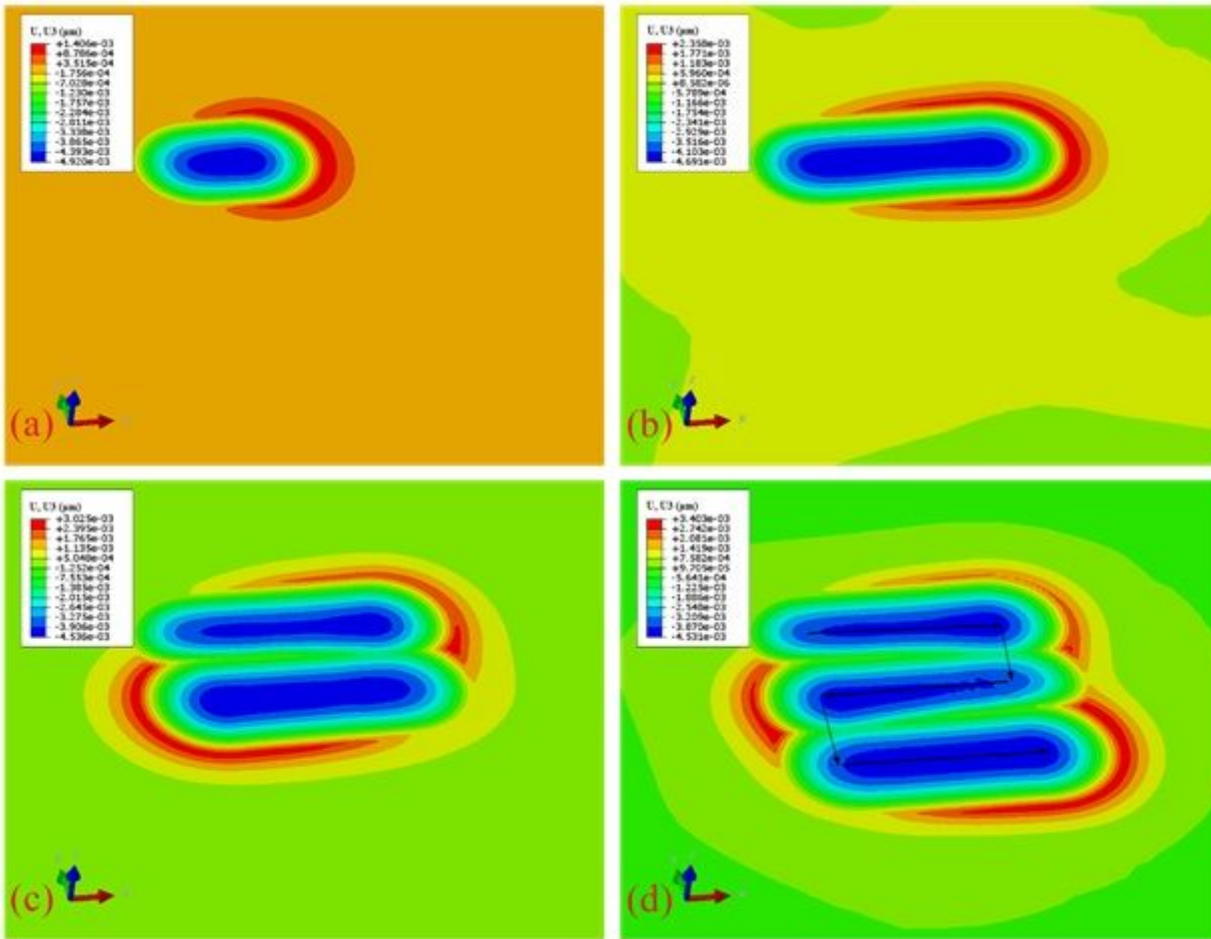


Figure 7

FE simulation of surface morphology evolution in continuous impact process. (a) Start processing, (b) one groove, (c) two grooves, (d) three grooves.

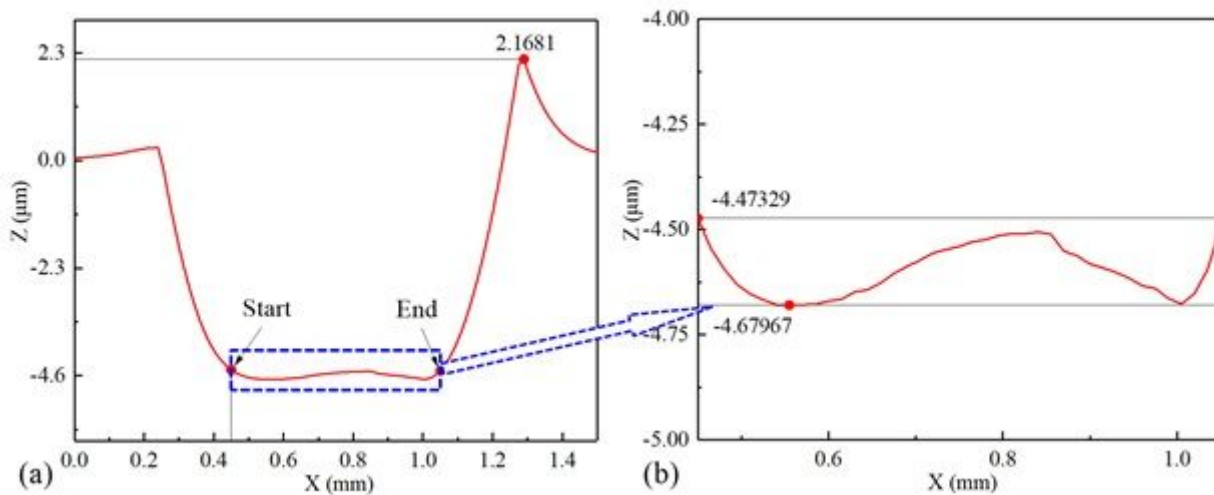


Figure 8

Morphology of groove bottom surface by using UIP. (a) Groove profile along groove direction; (b) Enlarged view of groove bottom.

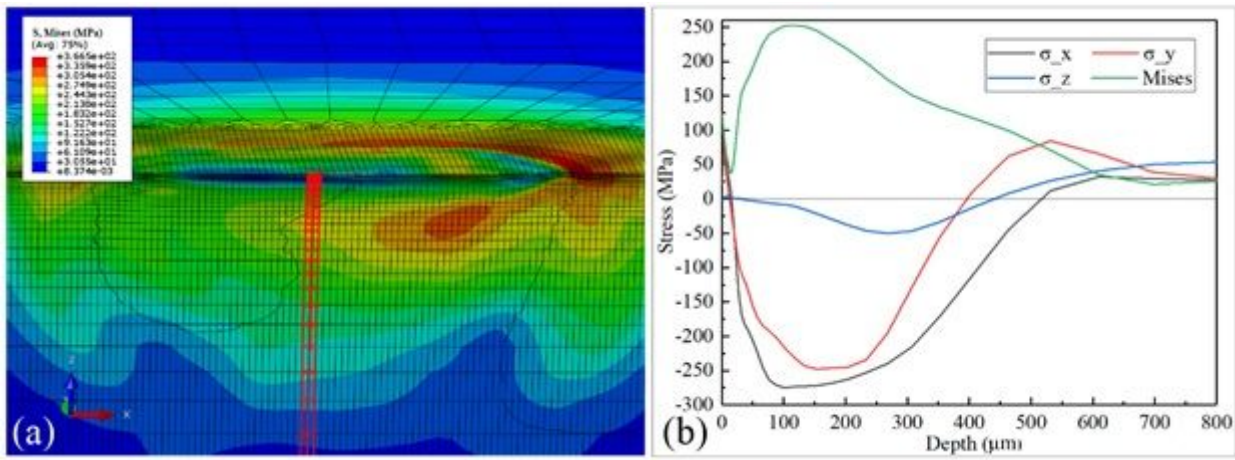


Figure 9

Stress distribution at different depths at the groove bottom. (a) Mises stress distribution; (b) Variations of residual stress with depth.

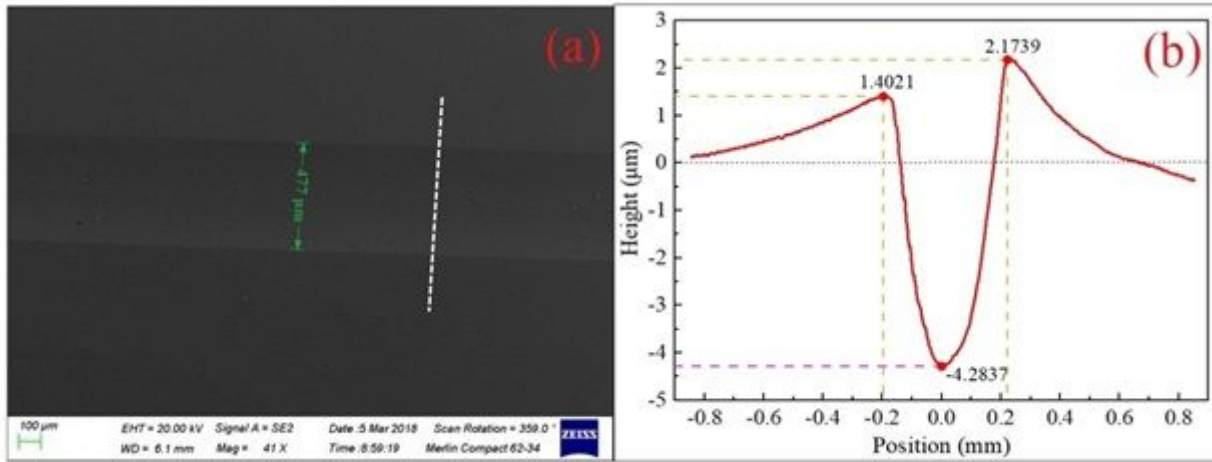


Figure 10

Morphology of single groove by using UIP. (a) SEM image of groove morphology; (b) Groove profile.

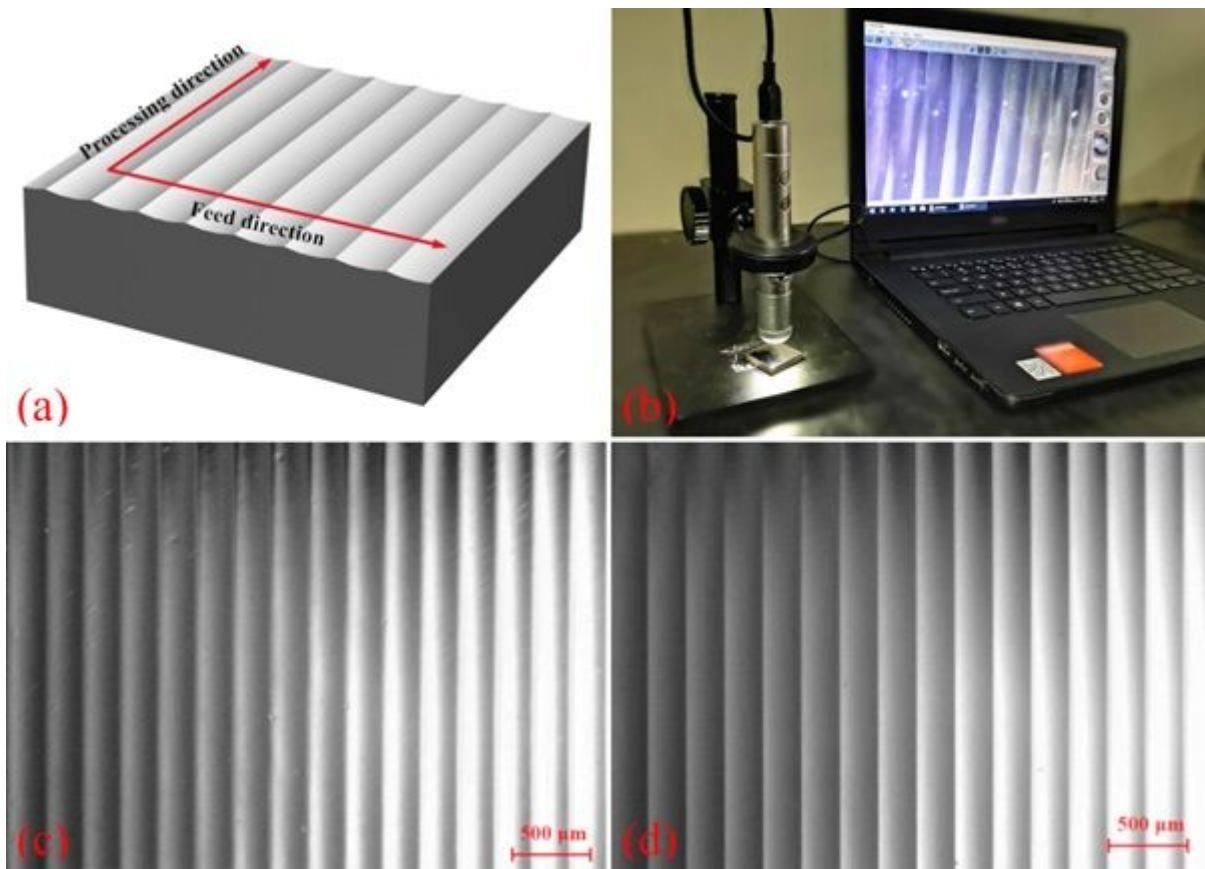


Figure 11

Micro-structures composed of aligned grooves fabricated on 316L stainless steel. (a) Schematic illustration of micro-structures fabrication strategy; (b) Characterization of micro-structures by an optical microscopy; Fabricated micro-structures by using (c) UIP and (d) UEVC.

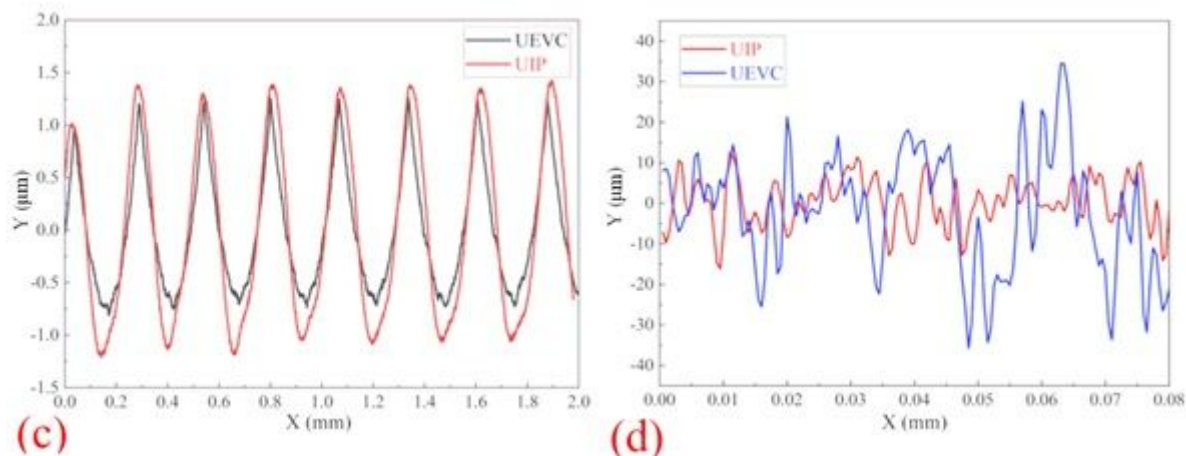
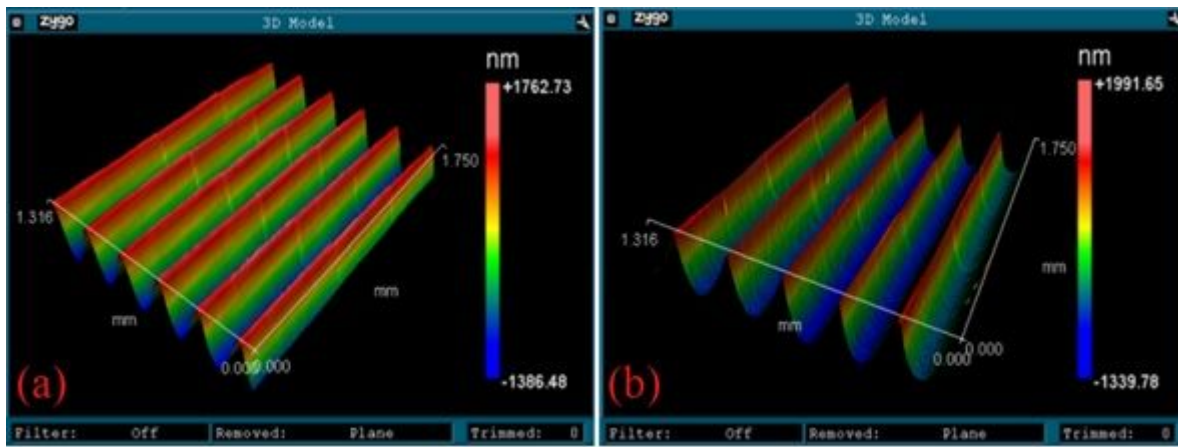


Figure 12

Geometrical features of as-fabricated micro-structures on stainless steel. Morphology of groove by using (a) UIP and (b) UEVC; (c) Surface profile of grooves; (d) Variations of groove bottom surface height.

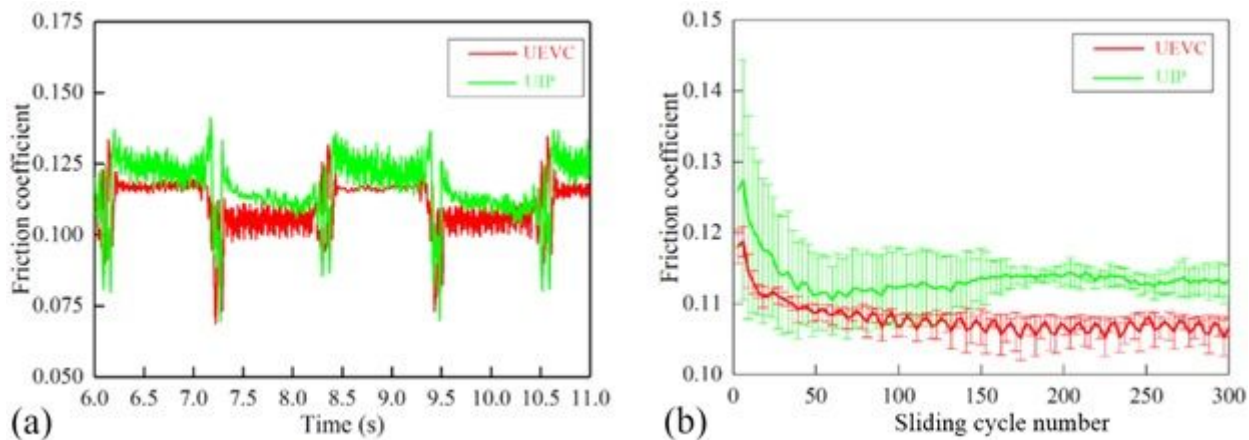


Figure 13

Frictional properties of as-fabricated microstructures. (a) Variations of friction coefficient within 2 sliding cycles; (b) Variations of average friction coefficient within entire friction test of 300 sliding cycles.

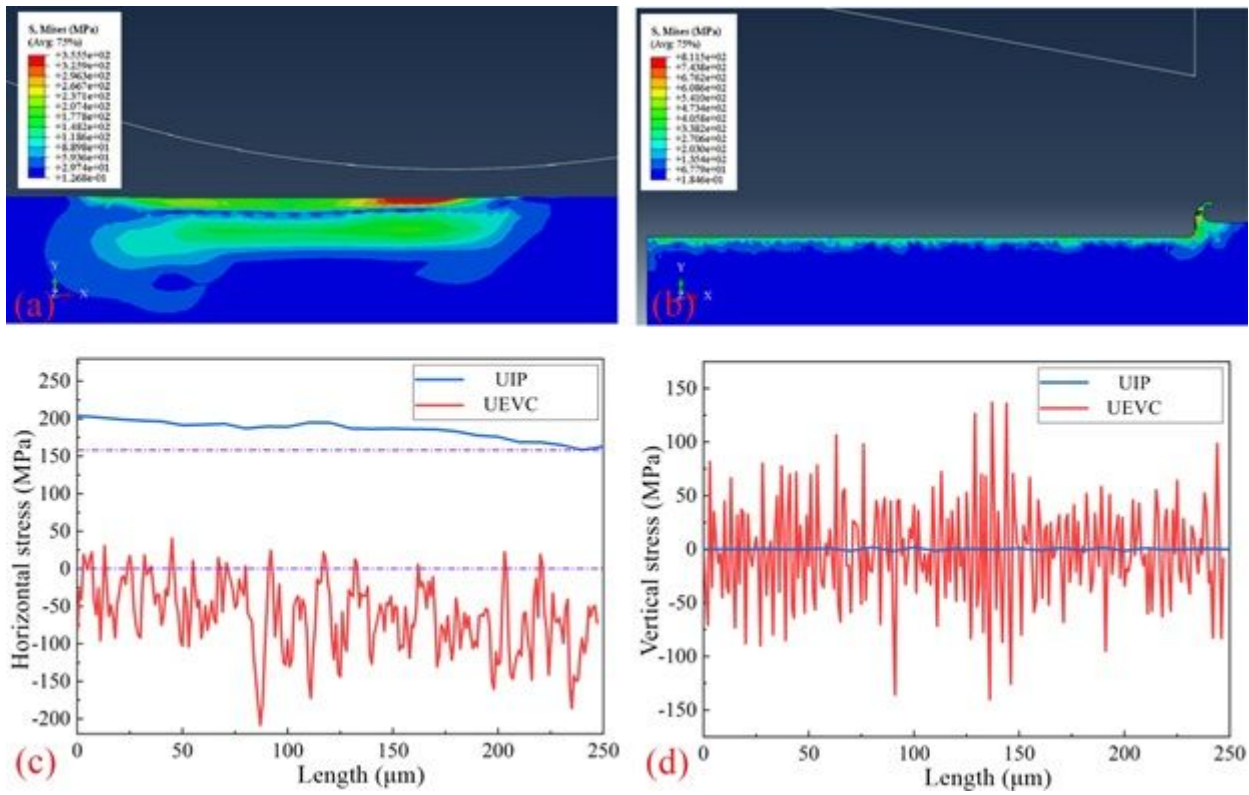


Figure 14

Cross-sectional residual stress contour of specimen treated by using (a) UIP and (b) UEVC; Variation of residual stress in (c) horizontal stress and (d) vertical stress.